Article

Structurally Controlled Landscape Evolution in Kula Badlands, Western Turkey

Selçuk Aksay [1,*], **Jeroen M. Schoorl** [1], **Antonie Veldkamp** [2], **Tuncer Demir** [3], **Ahmet Serdar Aytaç** [4] **and Darrel Maddy** [5]

1 Soil Geography & Landscape Group, Wageningen University & Research,
P.O. Box 47, 6700 AA Wageningen, The Netherlands
2 Faculty of Geo-Information Science and Earth Observation (ITC), Twente University,
P.O. Box 217, 7500 AE Enschede, The Netherlands
3 Geography Department, Faculty of Letters, Akdeniz University, Antalya 07058, Turkey
4 Department of Geography, Harran University, Şanlıurfa 63300, Turkey
5 School of Geography, Politics and Sociology, Newcastle University, Newcastle upon Tyne NE1 7RU, UK
* Correspondence: selcuk.aksay@gmail.com

Abstract: Badlands are extensively eroded landscapes consisting of weakly consolidated deposits within highly dense drainage systems. Their controlling and shaping factors can differ in relation to various internal and external conditions and processes that are not always well understood. This study focuses on the development of a badland landscape affecting Miocene and Quaternary sand-clay sediments in the extensional tectonic regime of Western Turkey with a multidisciplinary approach. The area between Kula and Selendi towns exhibits a badland topography with extensively eroded surface features, deepened gullies within poorly consolidated, sand clay-sized sediments. The results of structural field mapping and morphometric analyses using a 5 m resolution DEM to study the role of structural control in the development of badlands are presented in this study. Field data analysis supported by the quantitative assessment of longitudinal gully profiles illustrates the role of pre-existing structures as faults, their orientation and geometry in net erosion-sedimentation and the development of deepened gully networks. Representative illustrations, field photographs and block diagrams are presented to show the relationship between the rock structure and badland landscape. The connection between the extensional tectonics, erosional dynamics and geomorphology point to a structurally-controlled landscape in the Kula badlands in Western Turkey.

1. Introduction

Badlands are typically characterised as terrains with highly erodible, poorly consolidated, clay- and silt-size sediments, steep slopes, minimal vegetation, and high drainage density [1]. As earlier research suggests, intensive erosional processes leading to the development of badlands are often associated with the role of lithology [2], base-level change due to local uplift or volcanic damming [3–5], Anthropocene influence (e.g., poor land management) [6,7], climate change (i.e., extreme rainfall) and land degradation [8–10]. Although the origin and development of badlands have been of global research interest by various geoscience disciplines for many years, the role of structural control in badland formation dynamics as a controlling or conditioning factor is not yet widely reported [11–14]. There are only a number of studies that investigated the influence of base-level change and structural control combined with rock type influence in badland development [3,15–17].

Primarily, it is essential to have a good understanding of internal and external processes that lead to the development of such erosive badland landscapes. The complex interaction between the rock structure and surface dynamics is known to leave a specific imprint on the topography [18], and changes the mode of sediment transport and sedimentation

dynamics [19,20]. In particular, the sediment transport and deposition dynamics in river or deepened gully systems along fault zones may occur in response to the fault dynamics [21–23]. The influence of structural geology as a specific controlling factor is expected to lead to non-random erosion-sedimentation at predictable locations and certain morphological patterns. Without this specific control, erosion and sedimentation dynamics are linked to a transport capacity until a local dynamic quasi-equilibrium is reached [24]. Consequently, this would lead to randomly migrating locations of erosion and depositional zones. These two processes, resulting in predictable or random erosion-sedimentation locations and certain morphological patterns, may play an essential role in the development of such extensively erosive badland settings.

It is crucial to address these problems with a multidisciplinary approach by combining thorough geological and structural field mapping with morphometric analysis. However, there is a paucity of research investigating the interaction between the rock structure (i.e., the orientation of fault and bedding planes and their geometry), and Quaternary erosion-sedimentation dynamics that eventually lead to gully and badland development. The paucity is often related to the lack of detailed structural mapping. This multidisciplinary approach could provide a better understanding to reconstruct neo-tectonic activity and its morphological expressions in a landscape [25]. One way to analyse tectonically-induced landscape evolution is the quantitative assessment of the gully or river response to certain changes (e.g., lithology, faulting, gradient change or human interference) expressed with steepness indexes such as stream length-gradient (*SL*) index or normalised length gradient (*SLk*) index [26,27]. Similar methods have been applied to examine and demonstrate the geomorphological evolution of rivers in relation to fault activity and the geology of different regions of various scales over the past decades, and have provided insights into our understanding of deformation patterns [28–32]. One specific area, where the interaction of badland surface dynamics versus rock structure and faulting could be investigated, is the Kula Basin in Western Turkey (Figure 1A).

We hypothesize that the rock structure and its geometry in the extensional tectonic regime of the Kula Basin have a significant influence on the observed pattern of erosion-sedimentation dynamics and related landscape change. In order to test this hypothesis, we first mapped local rock units and faults in detail as well as Quaternary erosion and deposition sites within the gullies. Later the structural information was combined with the morphological and sedimentological properties of gullies to examine to what extent the badland development is structurally controlled in the Kula Basin. Morphological features (e.g. gully orientations) were further examined with morphometric analysis such as aspect-slope diagrams and normalised *SL* index analysis superposed on the detailed structural map of the study area.

2. Study Area

The Kula Basin is situated in the Kula Volcanic Province (Figure 1B) within the Kula-Salihli Volcanic UNESCO protected Global GeoPark [33]. The Kula Volcanic Province, the youngest volcanic area of Turkey, has been subjected to many geological, geomorphological and geochemical investigations, and is known for its Pleistocene and Holocene scoria cones and lava flows [34–42]. Earlier studies provided essential information on Quaternary sedimentation and surface dynamics of the Gediz River and its tributaries [40,43–47]. The geomorphological features of the Gediz valley have also been emphasised, and lavas of the Kula Volcanic Province have been previously mapped [34,39,48,49]. However, not much is known particularly about the badland topography, gully development and their possible controlling factors.

The study area is characterised by extensively eroded surface features, deepened gullies, badland slopes and dome-shaped forms on relatively poorly consolidated clay to sand-sized sedimentary rocks (Figure 2) bounded by the stratigraphically younger Quaternary basalt plateaux on the southern high end, and a limestone plateau in the north (Figure 3). The Quaternary volcanism-related several volcanic necks are also found near the basalt plateaux. The gullies drain into four main catchments of the Gediz River (Figures

1B and 3), namely the Selendi, Geren, Bozlar and Hudut in the Kula Basin. The gully erosion and bedrock incision are the most intensive in clay-silty sedimentary units. The villages and agricultural fields, which are situated on relatively flat plateaux (i.e., possibly the remnants of a former landscape), have not yet been extensively affected by the extreme erosion dynamics and bedrock incision. The northern carbonate uplands and two southern basalt plateaux, namely Burgaz and Sarnıç, have marked expressions on the topography. These stronger and well-drained basaltic rocks serve as a protection cap and make the plateaux less prone to extensive erosion and bedrock incision, causing relief inversion. The heights of the basalt plateaux vary between 600 to 650 m, whereas the height of the carbonate uplands vary between 800 and 890 m. On the other hand, the heights of the most erosive internal part of the basin vary from 390 to 650 m (Figure 3). Western Turkey is under the influence of the Mediterranean climate with seasonal high precipitation, which is considered a moderate to high level rainfall erosivity factor [56]. The cumulative annual rainfall is reported to be ca. 600–700 mm [57].
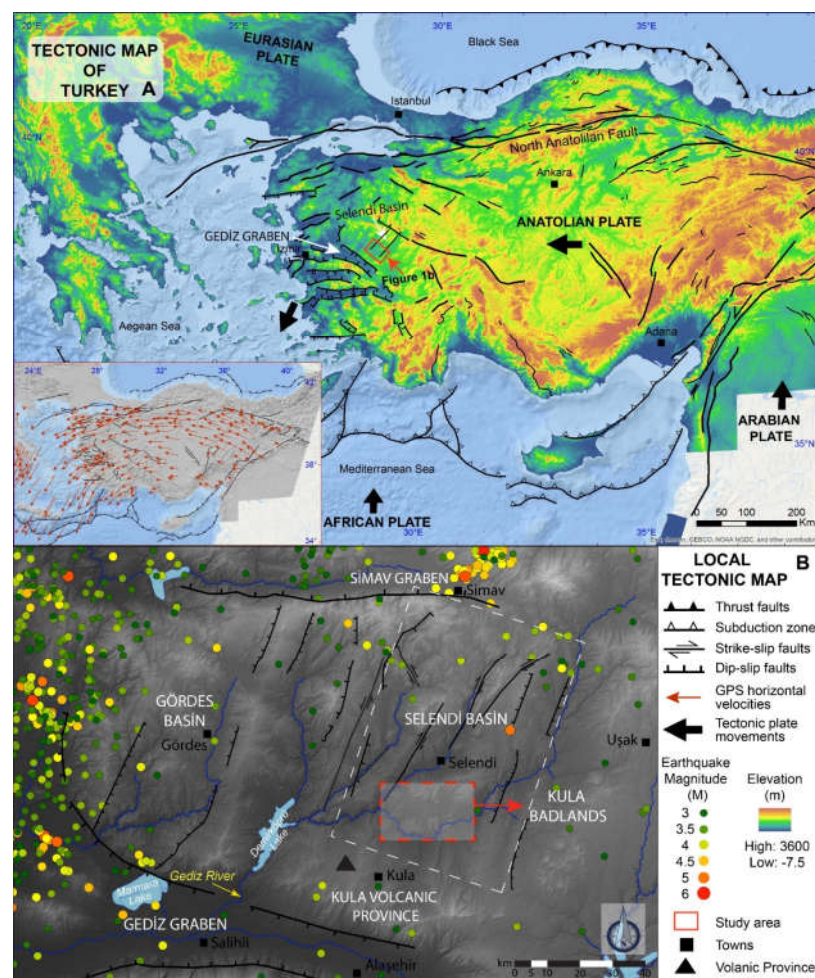

Figure 1. (**A**) Tectonic map of Turkey highlighting major tectonic units and showing location of the study area. Modified from [50–52]. The rotational tectonic frame with GPS-derived velocities modified from [53]. (**B**) Tectonic and location map of the Selendi Basin with major tectonic structures shown. Earthquakes of the past 40 years are also shown with magnitude. Digital Elevation Model at the courtesy of European Environment Agency (2020) [54]. Earthquake data acquired from USGS Earthquake Catalogue, 2020 [55].

Figure 2. General view of the badland topography and extensively eroded surface features. Red line differentiates the badlands from the limestone uplands (right).
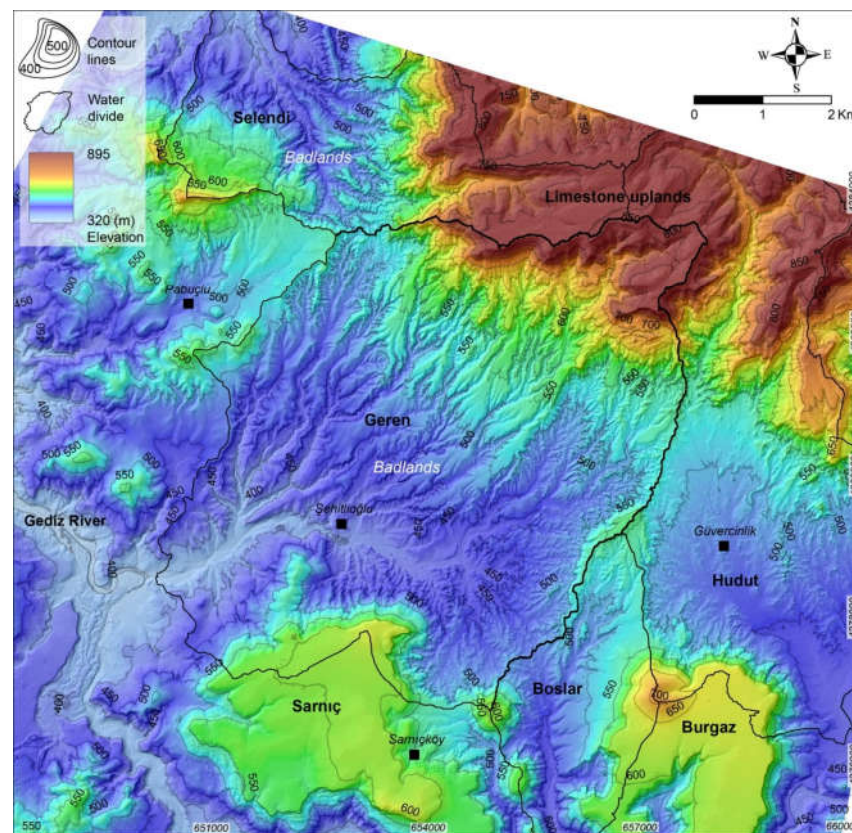

Figure 3. Topographic map of the badlands and the surrounding area showing erosive surface features, deepened gullies and water divides. Plateau and catchment names are indicated as well as village names.

Tectonic and Geological Setting

The Kula Basin is situated at the southern end of the Selendi Basin, in between the Gediz and Simav grabens (Figure 1B). The Selendi Basin is shown with major faults and earthquakes of the past 40 years [58]. The rock structure in the Selendi Basin has been under the influence of the extensional tectonic regime of the Anatolian-Aegean region [59–62]. The Anatolian-Aegean region has a unique tectonic evolution as it is in a convergence zone between the African, Arabian, and Eurasian plates [63]. It is controlled by a number of complex mechanisms; (a) the interaction of the African and Eurasian plates, causing the African plate to subduct beneath the Eurasian plate and the extension of the Aegean continental crust, (b) the dextral North Anatolian Fault (NAF), and (c) the collision with the northernly movement of the Arabian plate towards the Eurasian plate and the sinistral East

Anatolian Fault (EAF) movement [51,64–67]. The rotational westward movement of the Anatolian plate along the NAF and EAF with respect to Eurasia (Figure 1A) is the result of the pull and push escape mechanism [50,67]. The westward movement of the Anatolian plate, the extension of Western Turkey and the gravitational collapse of Eastern Anatolia are nevertheless more commonly associated with the relative role of Gravitational Potential Energy (GPE) differences (per unit area) and tectonic boundary conditions [68]. This work further substantiates the fact that the GPE difference is a major component of the total stress field in the entire eastern Mediterranean, parts of Western Turkey (NNE–SSW extension) and Eastern Anatolia. The role of GPE as a major driving factor in the lateral movement of the Anatolian block was also proposed in earlier work, based on the elevation difference between the East Anatolian Plateau and the Aegean Sea [69,70].

The origin of extension, deformation phases and development of grabens (e.g., Gediz Graben) in Western Turkey have been under debate, with several proposed models [42,60,62,71]. One of these proposed models suggests a continuous extension that began in the late Oligocene-Early Miocene [60,61]. The deformation of metamorphic and ophiolite rocks, outcropping only at the southwest of the study basin, refers to this early Miocene deformation phase. The overlying Hacıbekir group was reported to be partially tilted due to faulting, and folded due to the volcanic activity in the southern margin of the Selendi Basin [71]. Another geodynamic model proposes an episodic extension with three stages: an initial E-W extension, followed by two stages of N-S extension in the Miocene or post-Miocene [62]. A two-stage N-S-orientated extension model with an inactive phase in between was suggested to have occurred during the Miocene and stretching up to the Holocene [72–75]. Earlier studies also reported field evidence for broad folding on the southern margin of the Gediz Graben [75–77]. The origin of the folds was associated with both the N-S-directed compression [75] and the extensional tectonic regime of the Gediz Graben [76]. Despite the contradicting views and dispute on the origin of the folding, later work provided clear evidence that the fault-related folds were formed due to extensional tectonics [77,78].

In the Selendi Basin the Miocene extension-related deformation, as suggested in various models, was controlled by syn-depositional NE-SW-orientated sinistral faults and NW-SE-oriented dextral oblique normal faults [61] (Figure 1B). This phase refers to the post early Middle Miocene syn-kinematic deposition of the sediments of Ahmetler and Ulubey Formations in the Selendi Basin [74]. The lower sections of the Ahmetler Formation overlying the tilted and folded Hacıbekir group were reported to be tilted (i.e., covering the old landscape), whereas the upper parts were rather subhorizontal [43,60]. The Ulubey Formation carbonates were also described with their tilted layers along a gentle fold (i.e., axis of a syncline) [43]. The Late Miocene deformation later on modified the sedimentary deposits of the Selendi Basin with NNE-SSW-trending normal faults [42]. Further, the E-W-trending extension-related high-angle normal faults of possibly the early Plio-Quaternary age predominantly controlled the rock structure and the topography in the basin [60].

E-W normal faulting caused adjustments in the Gediz catchments generating shallow basins in the Early Pleistocene [45,46,48,79]. The catchment-wide changes were also influenced by climate control, associated vegetation, and lithology. Earlier research showed that previously identified Early Pleistocene river terraces were preserved beneath lava flows of the Sarnıç and Burgaz plateaux [45,79]. The higher terraces, which were not associated with contemporary volcanism, were reported to be older than the 1.3 Ma. volcanism. This terrace sequence was associated with reddish palaeosols and laminated calcrete development beneath the Early Pleistocene basaltic lava flows of the Burgaz plateau, as proposed by earlier work [80]. Reddish palaeosols beneath a densely vegetated environment were formed in possibly relatively humid conditions, and laminated calcretes were developed in more arid but cool environments (wet-dry cycles) before the 1.3 Ma. volcanism (an age estimate from the overlying lava flow) [48,79,80]. The younger terrace sequences were linked to localised active faulting (rather than a direct climate control) with the progressive downstream subsidence, which exhumes the basement topography [46].

Furthermore, multiple lava damming of the Gediz River had an influence on the transport-sedimentation dynamics. Multiple base level changes, including dammed lake phases and landslide deposition, changed the landscape in the Pleistocene-Holocene [4,38,81]. This translates into a continuously incising Gediz River and its tributaries (i.e., due to the overall tectonic uplift) being locally interrupted by lake phases and landslides, which affected the sediment transport in the landscape. Moreover, climate change as a conditioning or driving factor has also been emphasized for landscape development in the Gediz River system from the Pleistocene to the Holocene in previous research [37,79]. A recent study also suggested several wet periods which affected the agricultural practices of West and Central Anatolian people in the Byzantine Empire (4th–15th AD) [82]. These proposed changes in the climate most likely affected sediment transport dynamics in the Gediz River system and its tributaries by water erosion.

The local geological setting of the study area consists of the ophiolitic mélanges and the Hacıbekir Group at the bottom. Stratigraphically, the upper layer is the Ahmetler Formation, consisting of weakly consolidated continental clastic sedimentary rocks, with poorly lithified conglomerate and fluvial intercalations at the bottom. The cobbles and pebbles of fluvial sediments in the Ahmetler Formation are the fragments of the underlying ophiolitic mélange and Hacıbekir Group. The uppermost units of the Ahmetler Formation consist of sandstone and claystone. The development of the erosive badlands is commonly observed in these clay-sized and poorly consolidated sedimentary units [60,83]. The age of the Ahmetler Formation is of Early to Middle Miocene based on ^{40}Ar/^{39}Ar age estimates from tuff units [60], and this formation lies unconformably on top of the metamorphic basin. A carbonate plateau, mostly consisting of limestone and travertine, is stratigraphically located on top of the Ahmetler Formation in the northern boundary of the study area. This Miocene carbonate succession (i.e., the Ulubey Formation) consists of limestone, carbonaceous muds and silts, travertine layers and lacustrine facies [39,46]. Transitional sedimentation is observed between the Ahmetler and Ulubey Formations, with sandy-carbonate layers in the north of the study area. The uppermost layer consists of Quaternary basaltic flows and sedimentary units unconformably lying on the Ahmetler Formation on the southern end of the basin. The Quaternary sediments in the basin were interpreted as debris flow deposits and alluvial sediments [39], but were not mapped in detail previously. The preserved fluvial terrace staircase on the basalt plateaux is well studied [45,46,48,80], but only little is known about the lithological characteristics and sedimentation age of the fluvial and colluvial units of the badlands setting within the study area. Some Quaternary fluvial units at the southern boundary of the badland topography, consisting of fragments of the metamorphic basement, Ahmetler sandstone and Ulubey limestone are of the Holocene age based on OSL ages [4].

The badland morphology is recognised with extensively eroded surface features such as rills separated by ridges, gullies, and dome-shaped hill structures incising into clay-sized material in between basalt and limestone plateaux. The gully incision is commonly observed in sedimentary units of the Ahmetler Formation. This heterogeneity of Ahmetler sandstone and claystone in our badland setting is solely limited to clay silt-sized material. In comparison to the surrounding rocks (e.g., basalt), this heterogeneity does not strongly control the erodibility internally. The rapid upstream migration in the Geren and Selendi catchments also reflects the erodibility of Ahmetler sandstone and claystone [37,46].

3. Materials and Methods

Analysing the tectonic geomorphology of a basin in an approach by combining geological and structural mapping with examination of DEM-based morphometric parameters [84] provides an effective assessment. With this principle, we first started our investigation with morphological observations and mapping in the field to identify the badland area recognised within the steeply-incised gully systems. Slope aspect diagrams showing individual gully orientations and morphology were made to characterize the gully system. The morphometric analysis was further elaborated with normalised *SL* index analysis for

the Geren catchment. All morphological analysis were made on the GIS environment using a 5 m resolution DEM. The first detailed structural and geological maps were produced by extensive field surveys. Not much data on the rock structure and its geometry, particularly for the badlands area, is available in the literature. However, we combined the existing geological data from earlier work [39] with our geological mapping results to further elaborate our geomorphological investigation. Subsequently, gully properties, sediment characteristics and their occurrences were described and mapped in detail. Following our descriptions for the rock structure (faulting and folding) and gully morphology, we undertook further analysis to find out if there is any relationship between the development of gully systems and observed structural geology in the badland area. We additionally tested the proposed hypothesis that the preserved recent erosion-sedimentation are to some extent fault-related.

3.1. Geological and Structural Mapping

The geological and structural mapping were carried out systematically almost in every gully and in other available outcrops. For each outcrop, a handheld GPS device was used to record the UTM coordinates. All observations on the physical properties of lithological units, sedimentation structures and formation boundaries, measurements on bedding and fault planes were indicated on a geological map as the basis of this research. The lithological identification of rock units was established with hand specimens in outcrops and thin sections under a polarised microscope. A total of 12 thin sections were used to identify different solid rock units (Ahmetler sandstone–claystone and Ulubey carbonate rocks) and their physical properties, such as textural differences and grain size, using a polarized microscope. The azimuth and dip of fault and bedding planes were measured using a Brunton compass. Common kinematic indicators such as the orientation of fault planes, cross-cutting relationships and the position of hanging footwall were mapped to understand the sense of movement.

Possible cross-cutting relationships, syn-kinematic sedimentation and reactivated pre-existing faults were used to establish relative fault movement within the context of time and space. The indicators for syn-kinematic deposition are commonly observed in the form of fluvial wedge sedimentation. Fault plane orientations were further analysed with the help of rose diagrams using Stereonet 10.0 [85,86]. Additionally, equal area Stereonet plots were used to indicate the orientations of faults of each outcrop. Inferred faults (i.e., lineaments) were interpreted based on their topographic imprints observed in fieldwork and later studied using the 5 m DEM. Inferred faults make only 6–7% of all faults in the study area, and were not included in the rose diagram calculations and Stereonet plots. The lithological identification of rock units was made with visible physical characteristics in the outcrops including colour, texture, grain size, rock type and sedimentary structures. The geological boundaries between the Miocene rock units and Quaternary sediments were identified based on their lithological properties and sedimentation geometry as well. The Quaternary sediments were morphologically subdivided into two main units based on their position in the landscape (i.e., their heights from the current incision levels in the gullies): (i) plateaux sediments, (ii) intermediate gully sediments, and (iii) lower gully sediments found within the steeply-incised gullies. A cross-section demonstrates how these three different morphological units are linked in the landscape (Figure 4). These three Quaternary units were further differentiated and categorised based on their different provenances. (i.e., source of origin of pebbles and clasts), sedimentation geometries and thicknesses as well.

Palaeocurrent directions, inferred from primary sedimentary structures (e.g., imbrication, cross-stratification), were documented (when visible) for each sedimentary unit. Typically, the preferred orientation of pebbles or clasts (e.g., roughly 5–20 cm in length) dipping upstream was measured, indicating the opposite of the flow direction in palaeochannels. Imbrication measurements were corrected for tilting and further analysed with rose diagrams using Stereonet 10.0 [85,86].

All these descriptions were made with respect to differentiating rock units into individual lithostratigraphic units for mapping and correlation, and understanding erosion-sedimentation patterns in relation to faulting. Additionally, genetically similar sedimentary units were described following their lithological similarities and means of deposition and environment (e.g., energy, transport distance).
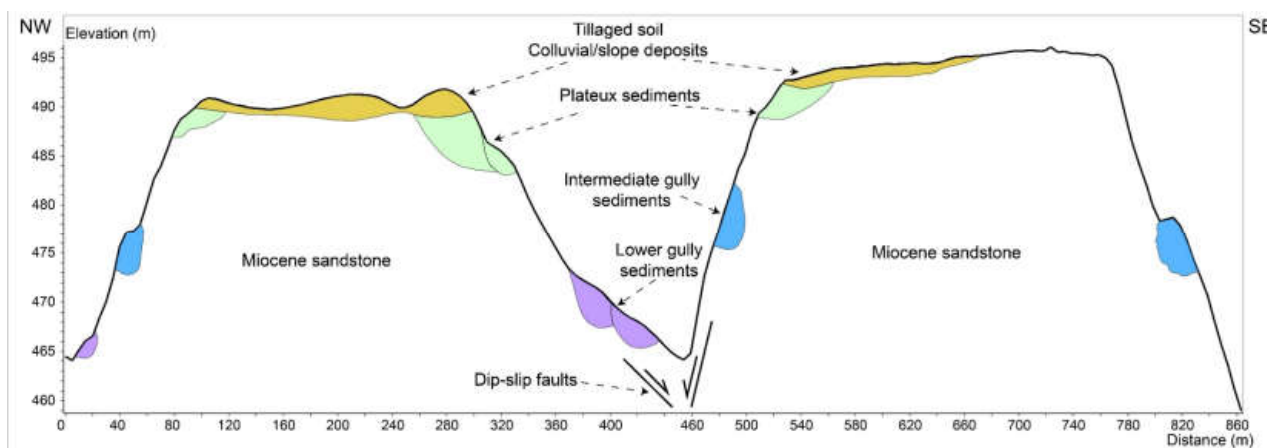

Figure 4. Morphological expressions of gullies-plateaux with observed sedimentation locations.

3.2. Morphometric Analysis

3.2.1. Aspect Maps (Gully and Badland Morphology)

Slope-aspect analyses were caried out to visually characterise the gully morphology and examine if there is any relationship between the observed faults and gully geometries and orientations. The input data for the aspect map production consisted of a 5 m spatial resolution DEM, with grid spacing of 5 m and accuracy of ± 3 m at a 90% confidence level from stereo aerial photographs. Calculations were performed using various tools on the GIS environment. A drainage map was generated using the Hydrogeology tool and aspect map using the Spatial Analyst tool. Aspects ware calculated using clockwise from north orientation and classified into 16 categories. Each category was assigned to an orientation. The results of these calculations were later plotted on rose diagrams to indicate the distribution of gully slope orientations.

3.2.2. SLk Analysis

To further elaborate our investigation on the behaviour of the gully topography in response to faults, the Stream Length Gradient (*SL*) Index [26] was calculated for the Geren catchment. The *SL* index is commonly used to show the level of change of gradient of a river or stream with respect to lithology, faulting or human interference, and is expressed in *SL* values [26,27]. The *SL* index is calculated for a segment of a given stream, using the equation by Hack (1973) [26]:

$$SL = (dH/dL)/L \tag{1}$$

where *dH* is the variation of elevation, *dL* is the length of the segment, and *L* is the total channel length from the midpoint of the segment where the index is calculated to the drainage divide.

In the Geren catchment, each sub-catchment profile has a short but different gully length, which makes it rather difficult to directly compare their *SL* index values, as also explained in a previous study [87]. To avoid this issue, we used the graded river profile *k* as a normalisation factor. By applying normalisation (*SLk*) following well-illustrated examples in the literature [32,87], we aimed at avoiding individual sub-catchments being affected by gully-slope changes and schematically demonstrate areas along mapped fault zones.

The *SLk* index values have been calculated using the same 5 m resolution DEM and variety of GIS tools, with a single flow drainage direction for each DEM cell with

a 16 directions (D16) method. This technique ensures that the flow is transferred from each grid cell in the direction of the steepest downward slope (i.e., adjacent or diagonal). Minor differences in the stream profile may result in deviations and fluctuations in the *SLk* values [29,32]. A variety of classification schemes are, therefore, commonly used to avoid background scatter [88–90]. Based on this classification, *SLk* values (from 0.1 to 80) were divided into 5 classes and each class was represented with a colour. Class 1 (green) represents *SLk* values between 0.1 to 5, class 2 (yellow) 5 to 14, class 3 (orange) 14 to 24, class 4 (red) 24 to 44, and class 5 (dark red) 44 to 80, respectively (Figure 5). Colours representing class 1 and 2 (green and yellow) were not indicated to simplify the map. The *SLk* index values were then superimposed on the structural map to examine the connection between gradient change and faulting.
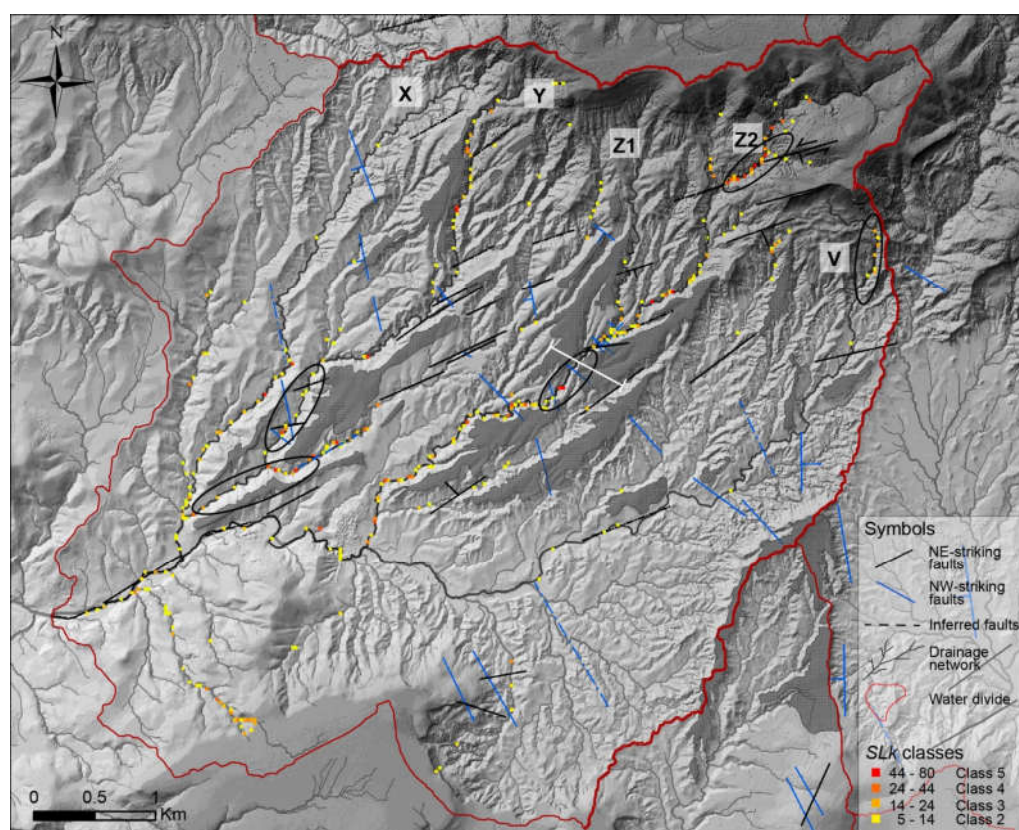

Figure 5. Morphology map with *SLk* indexes and NW and NE striking faults for the Geren catchment. Five gullies used for further visualisation are highlighted (X, Y, Z1, Z2, V, see text). Plateaux surfaces (dark grey) are indicated alongside the watershed of the Geren catchment. Circles indicate high *SLk*-index values (see text). Modified from [91].

4. Results

4.1. Gully Morphology: Badland Characterization

The gully topographies show similar morphological characteristics in the Geren and Selendi catchments. These two catchments are recognised by deeply-incised gullies in between elongated, often narrow and higher plateaux. The link between morphological expressions of these plateaux and incising gullies are shown in Figures 4 and 5. Despite certain similarities, the gully stream and slope orientations rather differ in the Geren and Selendi catchments; hillslopes in Geren predominantly point towards the southeast and northwest, and hillslopes in Selendi towards the southwest and northeast as shown on the morphology map (Figure 5) and in the rose diagrams for slope aspects (Figure 6). Gullies are also recognised with their steeper morphologies in the upstream catchment. Cracks and piping structures were also commonly observed towards the water divides. The badland

development occurs within gullies in between the plateaux, particularly in the fine grain (i.e., clay to silt) sediments of the Ahmetler Formation (Figures 2 and 7).
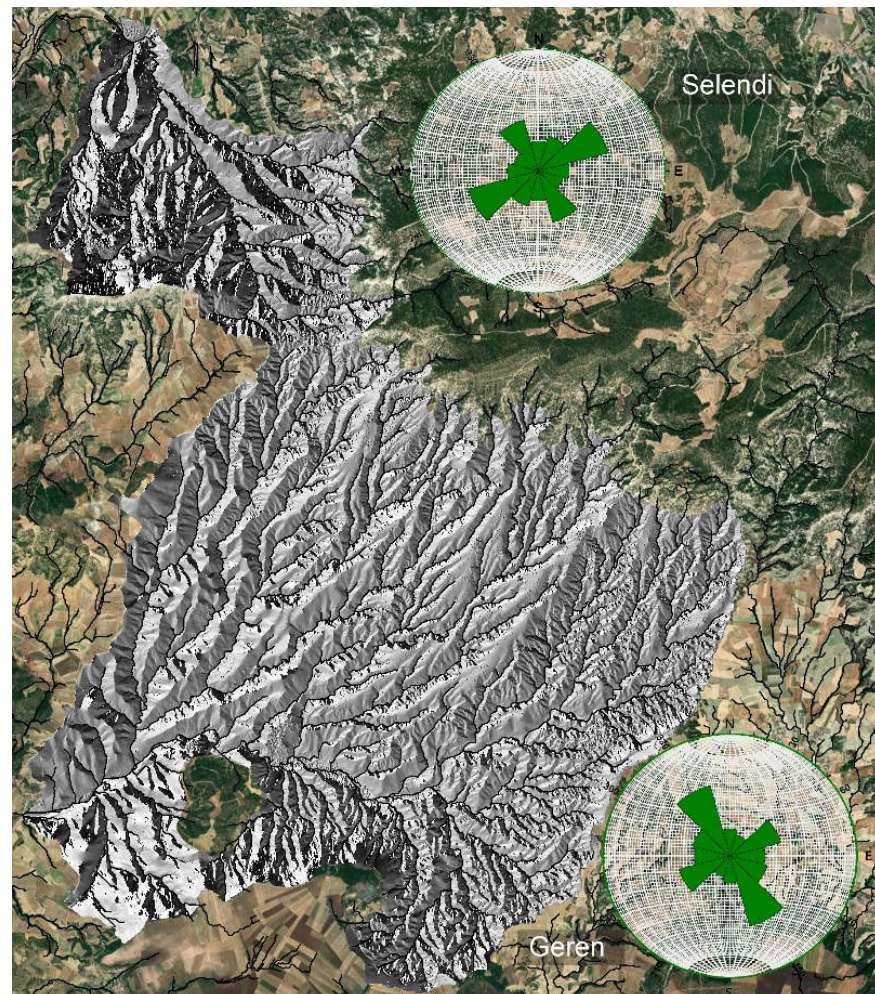

Figure 6. Shaded relief and slope orientations plotted on rose diagrams for Selendi (**upper left**) and Geren (**lower right**) catchments.

4.2. Rock-Type: Lithological Variety

As briefly introduced in the geological setting section, mapped rock units have been categorised into five major groups in our study area (from geologically older to younger rocks): (i) ophiolitic mélanges, (ii) Hacıbekir Group, (iii) sedimentary units of the Ahmetler Formation, (iv) carbonate rocks of the Ulubey Formation, and (v) Quaternary fluvial sediments and colluvial deposits. Basement rocks (i.e. ophiolites and rocks of the Hacıbekir Group) only crop out in a couple of locations at the southwestern end of the basin (Figure 7).

The rock units of the Ahmetler Formation are weakly consolidated, clay-silty continental clastic sedimentary units, as also indicated in earlier publications [40,60,83]. Additionally, a conglomerate layer with fragments of gravel to boulder size was mapped on stratigraphically the lower layers of the Ahmetler Formation only in a small area in the southwest of the study area (Figure 7). The Ahmetler Formation also consists of a local limestone unit up to a few meters thick only in one location (Figure 7). As mentioned in the geological setting, the Ahmetler sandstone is identified with its soft and readily erodible characteristics. In comparison to the underlying metamorphic rocks, most units of the Ahmetler Formation are relatively weaker. This makes these rocks prone to incision as observed in various gullies, particularly in the Geren and Selendi catchments. The relative erodibility of Ahmetler

sandstone and claystone can be directly observed in the rapid upstream migration in these clay silt-sized and unconsolidated rocks, as also indicated in earlier work [37,43,46,60,83].
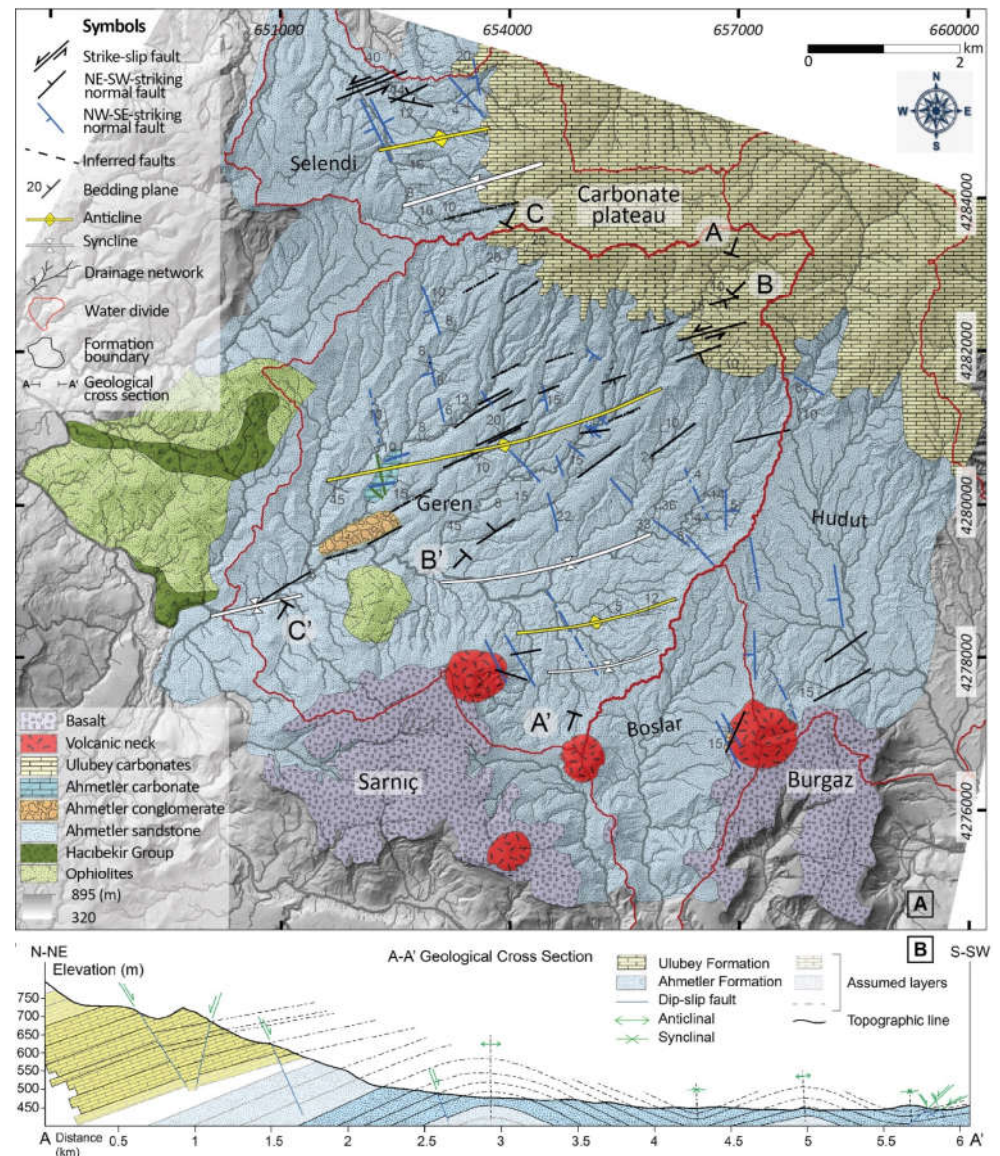

Figure 7. (**A**) Geological map of the Kula Basin with (**B**) cross section A-A' (other cross sections are shown with B-B' and C-C', see text). Faults are shown with blue and black lines. Strike-slip faults are shown with blue lines with arrows. Yellow and white lines indicate anticlines and synclines. Grid in UTM Zone 35 coordinates. Modified after [39,46,91].

From the Geren catchment toward the carbonate uplands, units of the Ahmetler Formation transitionally pass into sandy carbonate layers and limestones of the Ulubey Formation. The succession continues upwards with travertine layers and calcretes in places. The carbonate uplands consist of more relatively resistant rocks than the Ahmetler sandstone, and are less prone to erosion. Due to their visible relative lithological differences, the two rock units erode differently. Gully geometries between the two rock units also show differences due to their lithological characteristics. Gully slopes in the Ahmetler Formation seem to be more disturbed (i.e., unstable) and are extensively eroded due to their weakly consolidated and clay-rich lithological properties, whereas gullies in the Ulubey Formation are more stable.

4.3. The Rock Structure: Geometry of Faulting and Folding

The topographic expressions of faults and folds are indicated on the geological map and the cross-section A-A' (Figure 7). We observed fault displacements from several centimetres to meters in rocks of the Ahmetler and Ulubey formations (Figures 8 and 9). The greater fault displacements were observed on the steeper slopes of the carbonate plateau in the north, the basalt plateaux in the south boundary of the basin, and also in the internal parts of the basin. Some faults in the internal part of the basin were recognised by their topographic imprint and geometry of Quaternary sedimentation.
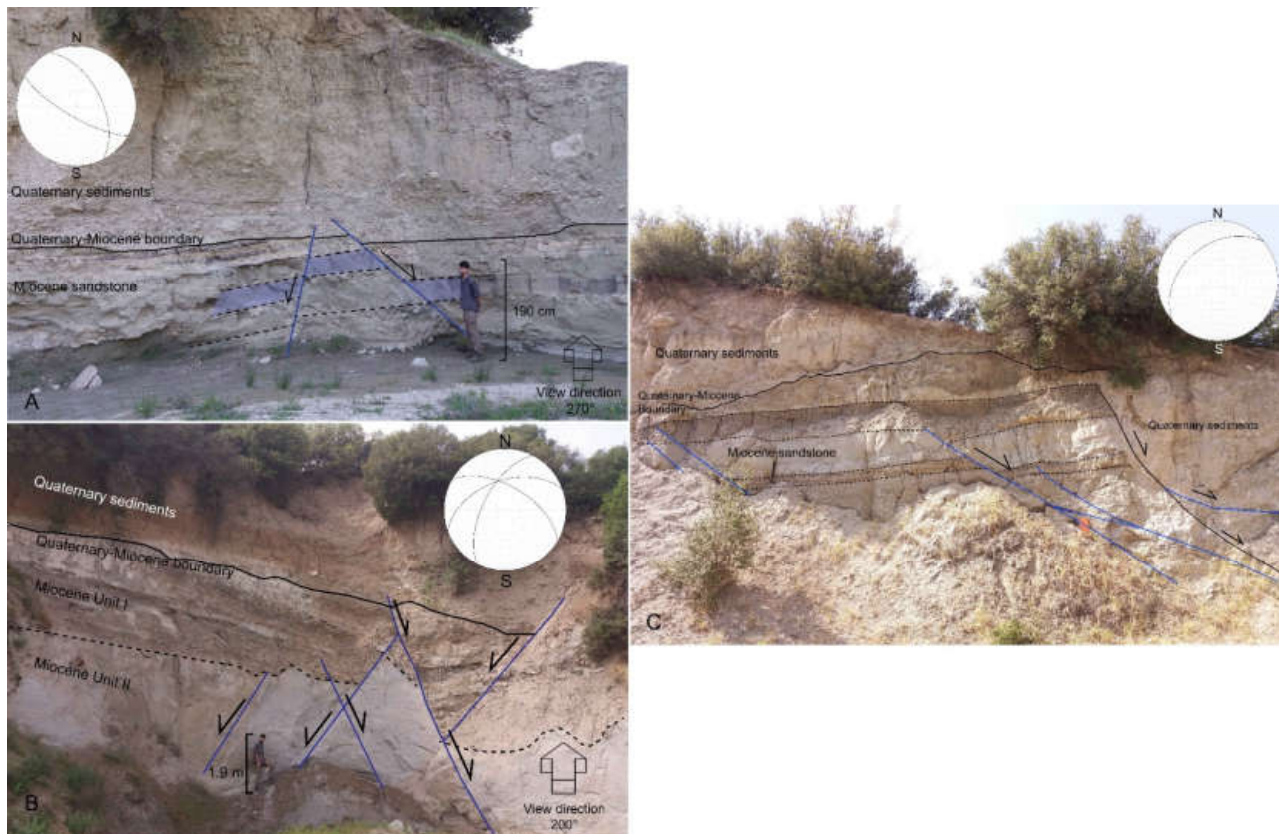

Figure 8. Field photographs showing two examples of extension-related normal faulting (**A**) 652190-4285123, 435 m, (**B**) 653864-4280877, 475 m, and listric faulting (**C**) 653217-4281021, 459 m. The fault propagation extends through different rock units in each photograph. UTM Zone 35 coordinate system is used.

We mapped two systematic sets of faulting with different orientations in the study basin. As the field observations imply, extension-related NW-SE-striking normal faults (blue lines), and NE-SW-striking normal faults (black lines) with an oblique component in some places, are commonly observed and measured in the Ahmetler and Ulubey Formations (Figure 7). NW-SE- and NE-SW-striking normal faults cross-cut specific sedimentary units of the Ahmetler Formation with a downward movement, implying the development of these faults at different extension stages from the Miocene onward.

NE-SW-striking faults are the primary normal faults in the basin, displaying a sinistral strike-slip component in two locations formed by the Middle Miocene extension [73]. The primary NE-SW-striking faults were followed by the secondary NW-SE-striking faulting in the basin, generating normal faulting with no observed oblique component. The NE-SW-striking faults crosscut both lower and upper sedimentary units of the Ahmetler Formation at different outcrops, which implies syn- and post-Miocene episodic fault movement. The secondary NW-SE-striking faults, however, do not crosscut all sedimentary units of the Ahmetler Formation (Figure 8). The fault geometry and relative cross-cutting

relationships show two phases of extension during and after the deposition of the Ahmetler Formation in the study basin, as proposed by earlier work [73,78,92]. The fault orientations and offsets are similar in the Ulubey and Ahmetler Formations.
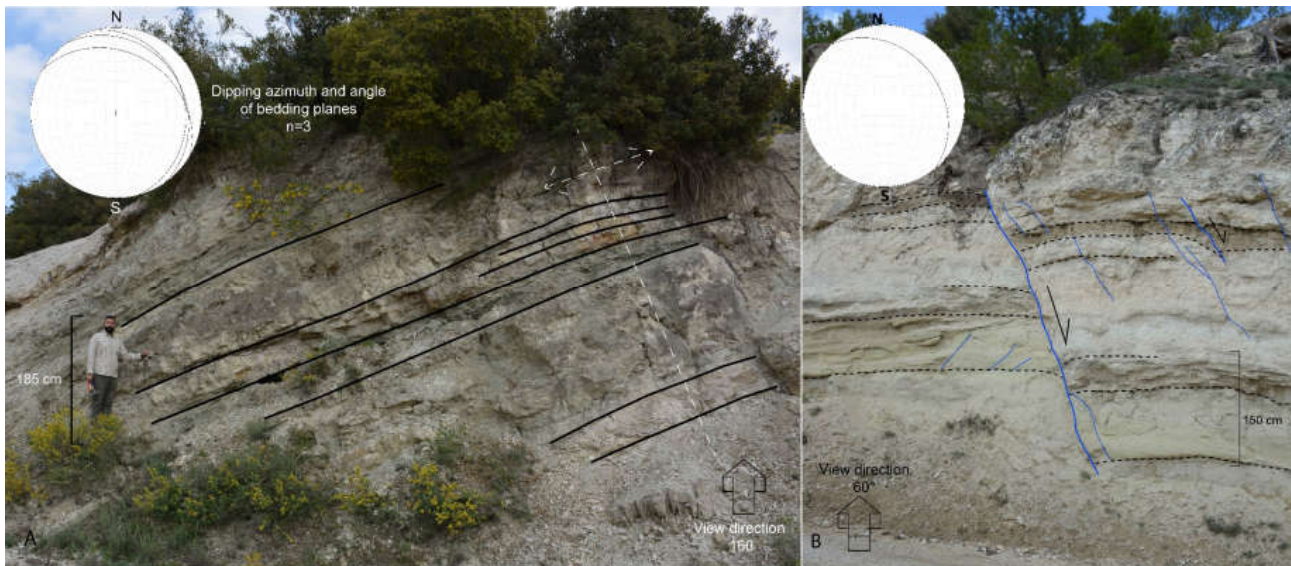

Figure 9. Field photographs showing folded, tilted and faulted bedding layers of the Ulubey limestone. (**A**) Dip azimuth and angle of the bedding planes are indicated on an equal area Stereonet. X-Y-Z coordinates: 653278-4285643, 528 m. (**B**) Dip azimuth and angle of the fault plane are shown on the equal area Stereonet. X-Y-Z coordinates: 656677-4282632, 724 m. UTM Zone 35 coordinates.

Although sedimentary units of the Ahmetler and Ulubey Formations appear generally subhorizontal in the field, the bedding measurements of these sedimentary units demonstrate a geometry of a gentle fold structure (Figures 7B and 10). Some tilted, gently folded and faulted beds can be observed on a macroscopic scale in the study area (see Figure 9). The orientation of fold limbs based on bedding measurements (see the geological cross sections and rose diagrams on Figure 10) implies asymmetrical gentle folding. The fold axes of anticlines and synclines can be seen on the geological map and cross sections (Figures 7B and 10). The dashed lines show assumed anticlines and synclines on the pre-erosion palaeotopography on cross sections. Typically, synclines form a basin with relatively concave geometry and topographic imprint. We observed a link between synclines and preferential water flow in the Selendi and Geren catchments. Particularly, the Geren catchment downstream (i.e., close to the southern boundary of the basin) follows the large concave pattern of the major syncline structure. These locations are indicated with white and yellow lines on the geological map, and dashed black lines with green arrows on the cross section on Figure 7. In addition, the water divide separating the Selendi and Geren catchments is along the limb of an anticline that serves as a barrier (with its relatively convex imprint) in between the two catchments (see the red lines on Figure 7). In addition to the bedding plane orientations, some areas in between the normal fault zones act as subsiding blocks, which might also influence preferential water flow in the present topography (Figure 10).
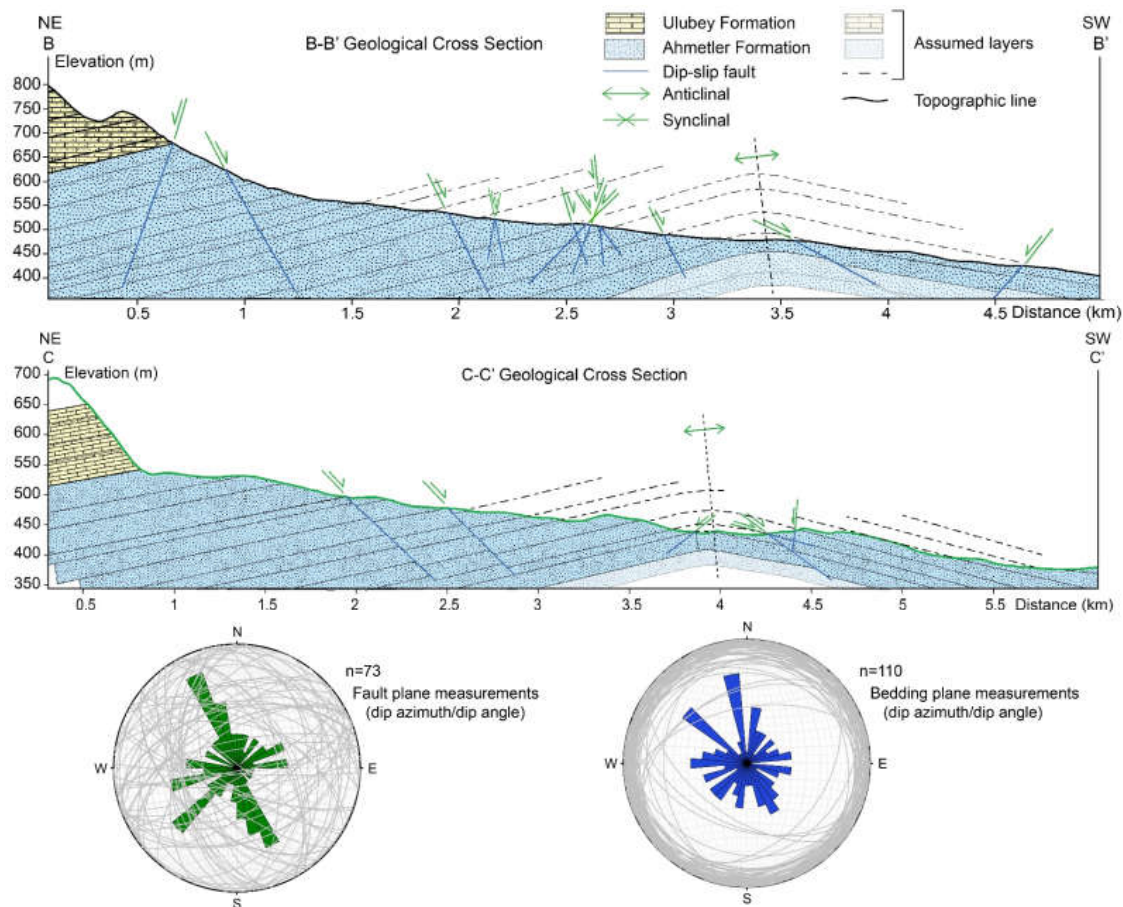
Figure 10. Geological cross sections of bedrock showing the fault geometry and rock structure. There is a vertical exaggeration. Both vertical and horizontal scales are indicated on each profile. Cross section locations are indicated with B-B' and C-C' on the geological map in Figure 7. Equal area Stereonets show: Left. Fault plane dip azimuth (green bar), dip angle (grey plots) of all fault measurements in the study basin. Right. Bedding plane dip azimuth (blue bar), dip angle (grey radial plots) of all bedding measurements in the study basin. Displaced fault blocks (typically a down-dip movement) were observed in between both NE-SW facing faults (cross section B-B'—the zone between 0.5–1.5 km) and/or SW-facing faults (cross section C-C'—the zone between 2–3 km). These subsiding block zones produce space for landscape adjustment in the present topography.

4.4. Quaternary Sedimentation

The youngest sediments in the Kula Basin are Quaternary deposits consisting of fragments of surrounding source materials, ophiolites, Hacıbekir Group, Ahmetler and Ulubey Formations and reworked Quaternary sediments. Quaternary fluvial sediments were observed with their poorly to well-sorted, mostly angular pebbles of calcareous origin (i.e., limestone, travertine of the Ulubey Formation), and/or rather rounded pebbles of metamorphic origin within a non-compacted sand- and/or clay-sized matrix. Pottery pieces of ancient and classical history eras (e.g., Lydian, ancient Greek, Roman and Byzantine) were observed within some fluvial sediments within the gullies in a few locations in the study area. Palaeocurrent direction indications in the form of imbrication and cross-lamination were also measured when visible.

Morphologically, Quaternary sediments were initially divided into three categories based on their position in the landscape (i.e., lower and middle gully, and plateaux sediments). Based on the lithological and grain size classification, these sediments were further subdivided into five groups. Clasts are bounded by clay- or sand-sized matrix in these fluvial sediments. These units are represented with their altitude on stratigraphic

columns. Their relative erodibility is also shown with width differences for each Quaternary unit (Appendix A).

1. Poorly-sorted fluvial sediments with clasts up to 3 cm of carbonate-metamorphic provenance.
2. Well-sorted fluvial sediments with clasts up to 20 cm of carbonate-metamorphic provenance.
3. Poorly-sorted fluvial sediments with clasts up to 3 cm of carbonate provenance.
4. Well-sorted fluvial sediments with clasts up to 20 cm of carbonate provenance (Appendix A).
5. Colluvium deposits.

The relatively thicker successions of Quaternary fluvial sediments were documented along or near normal faults (Figure 8 and Appendix A), typically on the hanging wall regardless their position in the landscape. The stratigraphic sections illustrate these zones of net sedimentation with the associated fault(s) with their fault plane orientations (Figure 11, Appendix A). The stratigraphic columns also demonstrate zones of no sedimentation or sediment preservation. These zones are located in the footwalls of NW-SE-orientated normal faults or NE-SW-orientated fault areas, where a great majority of deposits were eroded. Graded bedding and clastic wedges were observed, particularly along or near fault scarps, or occasionally on fault-associated fracture zones (Figure 12). These reported wedges thin and pinch-out in the hanging wall of normal faults, and some clasts or pebbles in the wedges dip towards the fault. The clast wedges uncomfortably lie above the incised Miocene sediments in the central parts of the Geren and Selendi catchments.
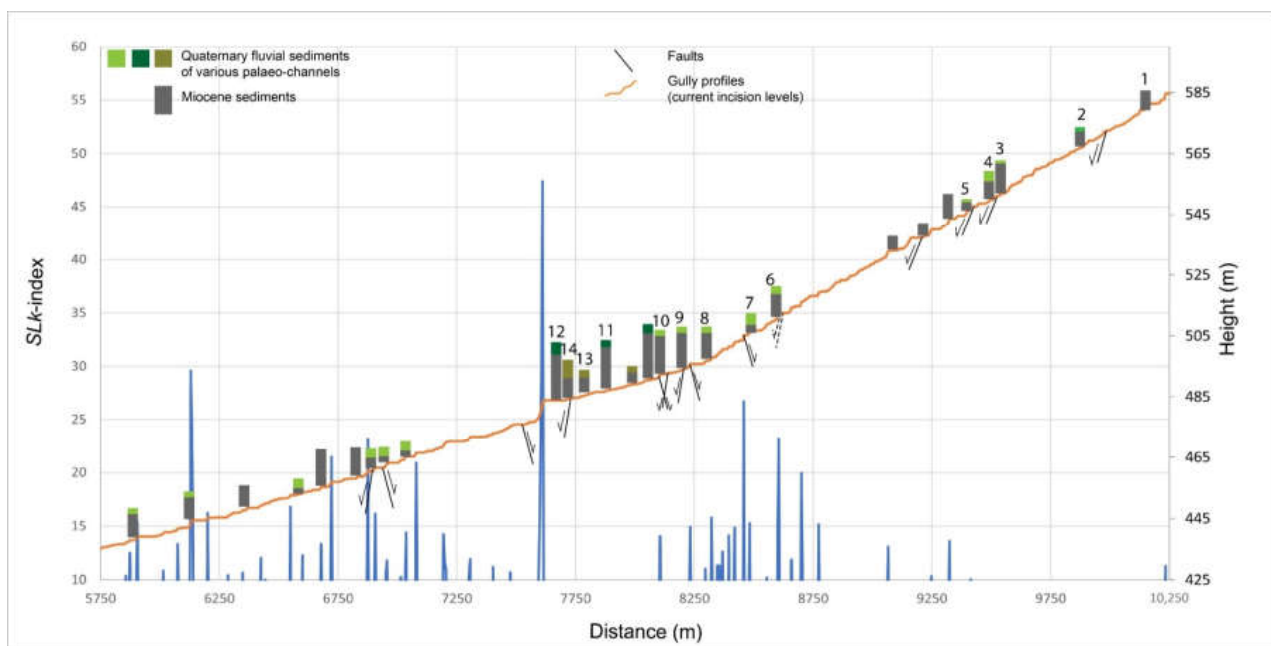

Figure 11. Stratigraphic columns of gully Z2 in Figure 5 showing correlation between eroded and deposited Quaternary sedimentary units along fault zones. Numbered stratigraphic columns are explained in Table 1. Faults are indicated with black lines between stratigraphic columns. *SLk* indexes for this selected gully also shown with blue lines. Modified after [91].

Figure 12. Clast wedges along fault scarps. Sedimentation is typically seen on the hanging wall in response to the footwall erosion. X-Y-Z coordinates: (**A**) 652573-4285333, 435 m. (**B**) 655015-4280973, 504 m. (**C**) 652625-4283997, 471 m. UTM Zone 35 coordinates.

4.5. SLk Indices and Connection to Faults

SLk index values were calculated for all gullies in the Geren catchment, and the data is visually shown in Figure 13 in graphs (see Figure 5 for map). All *SLk* values assigned to the catchment were superposed on the structural map of the area as well. Classes 1 and 2 were filtered out to avoid scatter, as mentioned in the methods and materials section. Classes 3, 4 and 5 correspond to mapped NW- and NE-striking faults and near inferred lineaments on the fault map (Figure 5). It is worth mentioning that some mapped fault zones do not correspond to any calculated high *SLk* index classes on the map. These mapped faults belong to older generation Miocene faults that do not propagate the upper Miocene units (as explained in the geological setting section), hence are not active. We also examined the formation boundaries of different rock units to check if they correspond to any *SLk* index classes. The boundary between the Ulubey carbonate upland and Ahmetler sedimentary units corresponds to a higher class in gullies Z2 and V (shown with a circle in Figure 5). We also mapped the NE-striking fault with a dip- and strike-slip component in this knickpoint location. Additionally, limestone and conglomerate boundaries at the lower level of gully Y are represented with higher *SLk* index classes as well (shown with a dark circle). We mapped a set of NW- and NE-striking faults in this limestone unit, and a NE-striking inferred fault on the conglomerate unit. We also detected a higher SLk index class corresponding to a man-made structure and a fault zone in gully Z (shown with a circle in Figure 5).
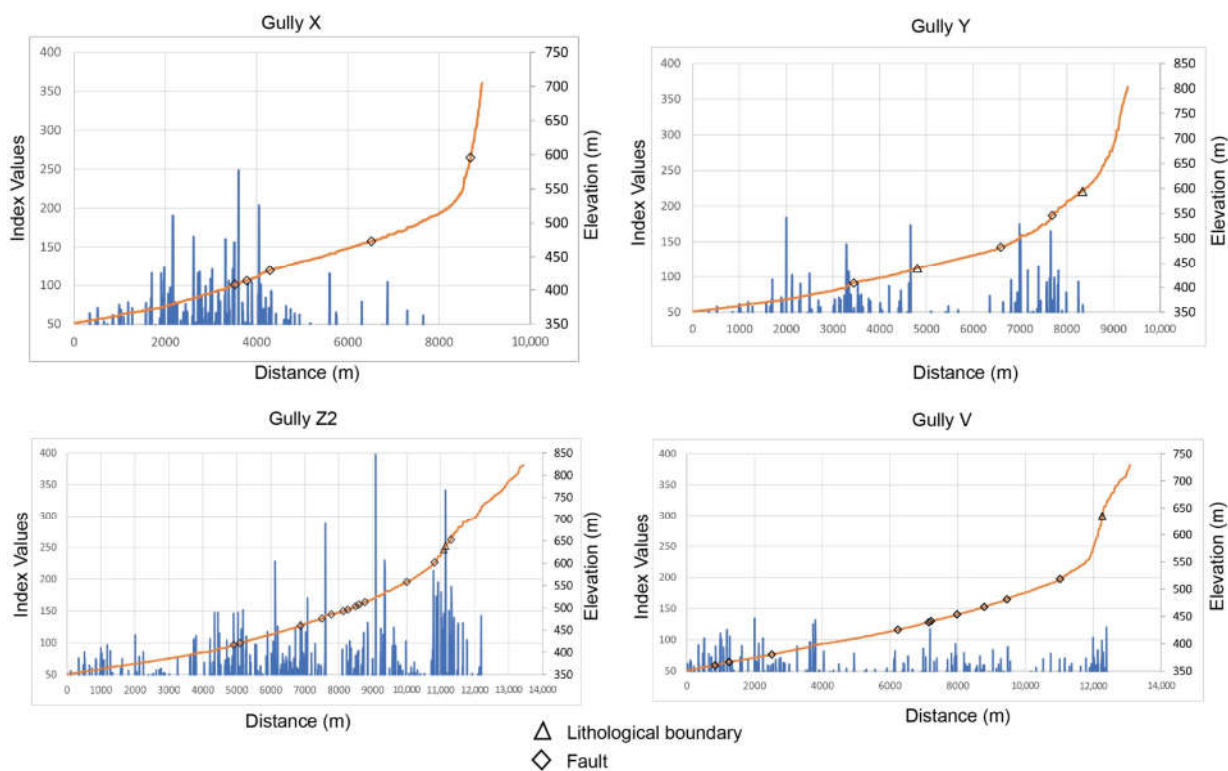
Figure 13. *SLk* indexes shown in longitudinal profiles for four gullies in the Geren catchment. See Figure 5 for selected gullies.

Furthermore, the correlated stratigraphic columns are indicated on a longitudinal profile, with stream gradient indexes showing the current incision levels on gullies X and Y (Figure 5), the thicknesses of Miocene and Quaternary sediments and their association with faults (Figure 11). Some of the higher *SLk* index values correspond to mapped fault locations and net erosion-sedimentation zones, as demonstrated in Figure 11. Eighteen locations were chosen to demonstrate the influence of faulting on erosion and sedimentation near fault zones in palaeochannels (Table 1).

Table 1. Correlated stratigraphic columns with erosion-sedimentation in relation to normal faults explained as given in Appendix A. Also see Figure 11 for the longitudinal profile with *SLk* index.

Stratigraphic Columns	Explanation
1, 2	Located on a steep slope. No Quaternary fluvial sedimentation was observed on column 1. Around a meter thick Quaternary fluvial sediments were observed on column 2 downstream. A NE-SW-orientated fault was present near these outcrops.
3, 4, 5	Demonstrate a similar drainage pattern along observed faults. The carbonate-rich Quaternary fluvial sediments were mapped in these outcrops, getting relatively thicker downstream along a fault scarp. Relatively higher *SLk* index values were observed in these fault zones.
6, 7	Higher *SLk* index values on the steeper part of the slope were observed on columns 6 and 7. Column 6 is located on a step-like surface near an inferred fault, which indicates more stability for sediment preservation. The carbonate-rich Quaternary sedimentary unit is around 1.5 m thick in length. In a similar example, the relatively thicker carbonate-rich Quaternary fluvial sediments (2 m) and colluvial sediments above (almost 2.5 m) were observed on column 7 near a fault. These two outcrops are located near a fault zone. The higher *SLk* index values also confirm this observation.

Table 1. *Cont.*

Stratigraphic Columns	Explanation
8, 9, 10	The carbonate-rich Quaternary fluvial sediments of coarse to fine grain size were observed on columns 8, 9 and 10 downstream. In particular, column 9 has a relatively thicker fluvial sedimentary unit, and both 9 and 10 have colluvial deposits on top. Columns 9 and 10 are near faults, as shown in Figure 11 and Appendix A. Rather higher *SLk* index values confirm this observation.
11, 12	11 and 12 display a rather different sedimentation pattern downstream on the less steep slope part of the selected gully. It must be noted that these two outcrops are located on the opposite side of the gully at relatively different heights. Colluvial deposits were observed above the Quaternary fluvial sediments on column 11. A relatively thicker Quaternary sedimentary unit was observed, but no colluvial deposits were reported on column 12 near a fault.
13, 14	Similarly, carbonate-rich Quaternary fluvial sediments were reported on columns 13 and 14 (about 3 and 6 m, respectively). The thicker Quaternary fluvial sediment package on column 14 is located after a NW-SE-orientated fault downstream. The *SLk* index value indicates a slight change in this fault zone as well.
15, 16, 17, 18	An additional four stratigraphic columns were selected in gully X (Figure 5). Columns 15, 16, 17 and 18 have various Quaternary–Miocene boundary levels and Quaternary sediment thicknesses. Columns 16 and 17 are located on a fault zone of two NW-SE-striking normal faults. Quaternary fluvial sediments consisting of pebbles of carbonate and metamorphic provenance seem to be inherited from column 15 upstream. These preserved Quaternary fluvial sediments are relatively thicker on columns 16 and 17 (i.e., both 2.3 m) compared to 15 and 18. Note that column 18 is located on a footwall, a zone of no sediment preservation.

5. Discussion

5.1. Quaternary Sedimentation and Erosion within the Context of Structural Control

Field data analysis (Figures 7, 9 and 10 and Appendix A) shows that the fault geometry plays a demonstrable role in net sediment accommodation and preservation. The fault geometry and matching fault-controlled Quaternary erosion-sedimentation patterns confirm a dynamic landscape influenced by the adjustments of an asymmetric mini horst-graben system, with extension-related faulting in the Kula Basin (Figure 14). This newly introduced mini-graben was illustrated in the tectonic block diagram with a conceptual erosive landscape, to demonstrate the ongoing relationship between faulting and the development of gully morphology, as explained below.

The extension-related faults form offset channels and gullies, causing strong control on erosional patterns in the study area. A similar case of extensional tectonics affecting gully deepening is shown for the Ganga Plain foreland basin, India in earlier work as well [17]. Furthermore, as shown with palaeocurrent indicators such as imbrication, palaeo-flow directions of the Quaternary channel fills predominantly point at southwest. As demonstrated in the rose diagram (Figure 15), palaeochannel flow directions (green bars) are in the same alignment as the dominantly NE-SW-striking relict and Quaternary fault system (note that the blue bars indicate the fault plane dip azimuth) (Figures 8 and 15). This is one of the primary observations that indicates the influence of fault control in the palaeochannel and erosion patterns regarding badland development.

Fault scarps of most NW-SE-striking normal faults play an essential role in erosion-sedimentation dynamics in individual gullies. We documented the net Quaternary fluvial sedimentation at fault scarps, typically along the hanging wall of normal faults in response to footwall erosion (Figures 12 and 16, Appendix A). The ridge of the footwall of normal faults are subjected to the fastest erosion, due to the exposed steep slope in the fault scarp (Figure 16). Therefore, the relatively thicker net Quaternary sedimentation occurs and is preserved on the hanging wall of the fault scarps, as the subsiding-hanging wall generates enough space to accommodate sedimentary deposits in response to the erosion on the footwall. In other words, preferential erosional surfaces along fault planes are associated with the systematic down-dip movement of normal faults. Once there is sufficient gradient between the footwall and hanging wall, fault-guided local erosion-sedimentation cycles occur in the basin. These sediment successions on fault scarps, if examined individually,

could also be considered slope material formed by small size mass movement on hillslopes rather than tectonically-induced sedimentation. However, these deposits do not have the internal structure that might indicate a mass movement origin. Additionally, we observed indications for fluvial sedimentation (e.g., imbrication) and synsedimentary structures (e.g., graded bedding, wedges) in these sedimentary units (Figure 12). These observations indicate syn-kinematic fluvial sedimentation, signifying the presence and influence of active tectonics in the Quaternary. Some preserved Quaternary erosion-sedimentation zones along faults may not only be linked to the deep-rooted extensional fault system of Western Turkey, but also the associated faults and fractures of the extensional fault geometry linked to the localised Quaternary fault adjustment of the Kula Basin.
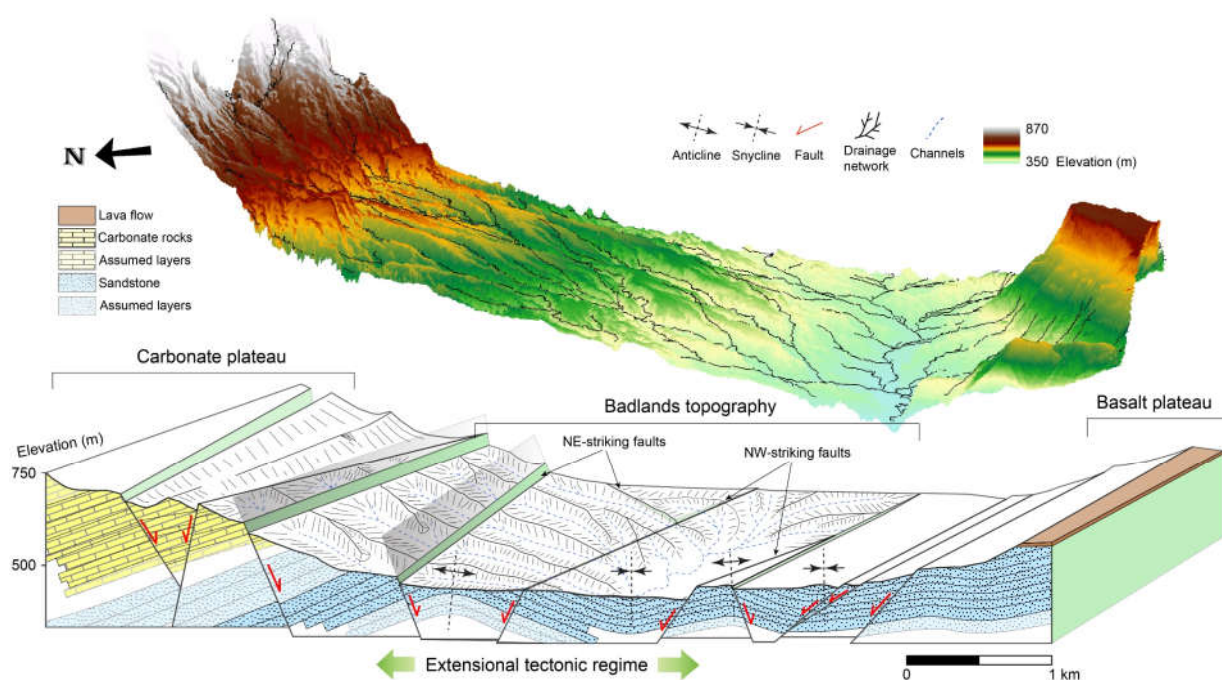

Figure 14. Tectonic block diagram highlighting extension-related fault development in the Kula Basin. Adapted from [91]. Rock structure and faulting are indicated with arrows. Actual fault and bedding measurements were used to construct the diagram. See Figure 10 for other cross sections and rose diagrams. The erosive landscape shown as a conceptual sketch is only to indicate the relationship between faulting vs. conceptual gully network.

The syn-depositional character of the normal faults is also recognised by the clast wedges along the fault planes, usually covered by fine-grained deposits (Figure 12). The development of clast wedges with a pinch-out shape, and the clasts dipping towards the fault along normal faults, also suggests syn-depositional fault influence, possibly with local listric fault geometry (Figure 8C) [93,94]. The clast wedges were observed on the internal parts of the basin, but not on the graben shoulders or upstream in the catchments. These are the locations where low-angle detachments and listric faults are locally observed in the graben system.

Palaeo-flow directions and erosion-sedimentation along fault zones evidently indicate a tectonic-controlled transport in the Kula badlands. This shows not only fault-guided Quaternary sedimentation, but also present-day sediment preservation and gully development. Although sediment yields are not quantitatively shown in this study, our results agree with earlier work suggesting that faulting and associated fracturing in rocks in tectonically active areas leads to an increase in contemporary sediment yield, as quantitatively shown [21,95]. The link between faulting and gully stream gradient change is supported with *SLk* indices calculatsed for the Geren catchment in our work. Our analysis of *SLk* index classes indicate that majority of actual faults correspond to high *SLk* index classes. Given the difficulty of

calculating *SLk* index values in a gully system with quite short travelling distances, these results are surprisingly good. Only a small percentage of older generation NW-SE-striking existing Miocene faults are not recognisable on the *SLk* index classes, since these are not active faults (Figure 8B). Additionally, some high *SLk* index classes coincide with zones of inferred faults (see dashed fault lines in Figure 5) or no-fault observations in the field. These inferred fault locations are covered by outwash colluvium deposits, which made it impossible to make direct observations in the outcrop. Yet, it is possible to see their topographic imprints in the field and DEM. Nonetheless, the inferred faults only make about 6% of the entire measured faults in the Geren catchment, which does not change our overall interpretation for high *SLk* index values. Along with the structurally-controlled erosion-deposition zones, there are a few randomly migrating erosion-deposition zones in the gully network as well [24]. Roughly less than 10% of the high *SLk* index values predictably coincide with randomly migrating depositional zones as well. The preservation of such few randomly migrating erosion-deposition zones is nevertheless expected in a gradient-determined gully network. Furthermore, *SLk* index calculations were made using a 5 m DEM with an accuracy of ± 3 m. We do not want to dismiss the likelihood of DEM background scatter for these zones of high *SLk* index classes as well.
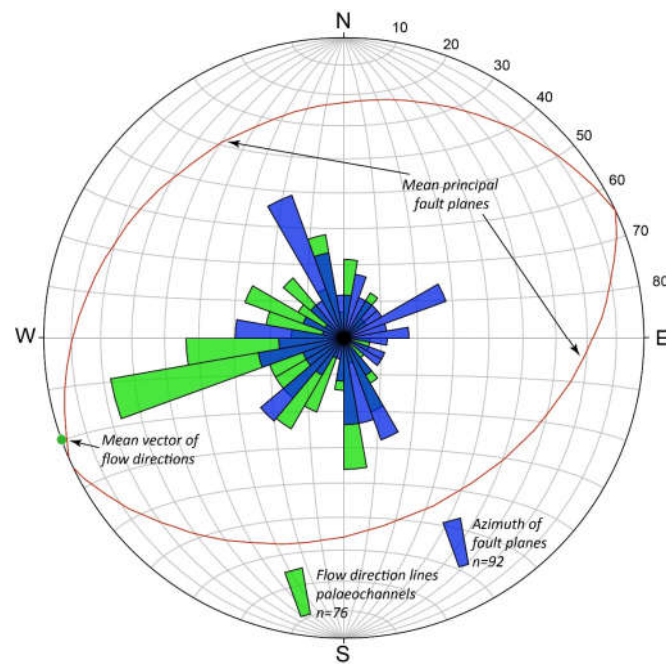

Figure 15. Projection of dip azimuth of NE-SW-striking fault planes and palaeochannel flow directions (opposite of pebbles dipping upstream) on an equal area rose diagram. Mean vector of flow directions (SW-W) versus mean dip azimuth of fault planes (NW-SE) are shown to indicate the preferred water flow orientation in palaeochannels.
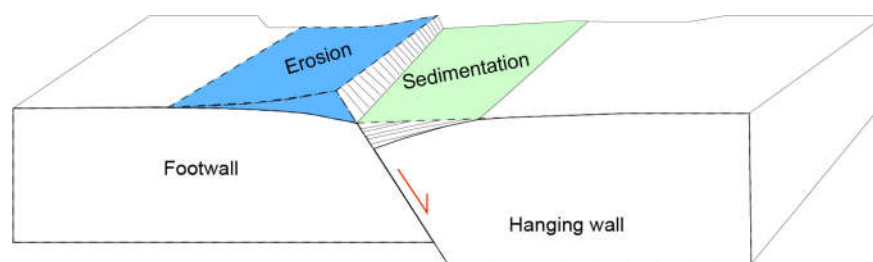
Figure 16. Symbolic erosion-sedimentation model on the footwall and hanging wall of normal fault. Sediments are deposited on the hanging wall of a normal fault in response to footwall erosion. Typically, syn-kinematic wedge sedimentation geometry is also observed in these fault zones (Figure 12).

5.2. Structural Control in Gully Morphology and Badland Development

Present gully stream directions (i.e., roughly perpendicular to gully slope orientations) in the Geren catchment are in the same alignment as the NE-SW trending fault lines (Figures 5, 7 and 15). This indicates that these faults predominantly control the topography and serve as a preferential set of patterns for water and sediment transport, both in Quaternary and present topographies. The folding structure, represented by tilted and gently formed beds (i.e., anticlines and synclines), also has an influence in present-day gully morphology. This locally observed fold structure, which may be associated with the existing inherited rock structure, plays also a discernible role in erosional patterns in the Kula Basin.

Theoretically, alternating erosion/sedimentation cycles along a steep gradient due to upstream migrating incision and downstream migrating deposition zones lead to badland development [24]. Without a specific control, this would lead to randomly migrating locations of erosional and depositional zones, and their long-term preservation in a dendritical drainage system. Our structural examination on the Kula Basin reveals that all studied catchments and their sub-catchments have preferential water flow directions (i.e., non-dendritical) in response to the geometry of faulting and folding. The syn-kinematic erosion-sedimentation cycles lead to a continuous rework mechanism within currently incising gullies at fault determined locations. This causes a rather complex but explainable imprint of depositional and erosive zones. The related gully development in between plateaux (Figures 4 and 5) bounded by faults eventually leads to the development of a unique badland topography.

In addition to local adjustment of the badland topography along the fault bounded locations, it is appropriate to mention the role of regional (i.e., Eastern Mediterranean and Eastern Turkey) gravitational potential energy difference, causing NNE-SSW trending extension in parts of Western Turkey as a known faulting and deformation trigger [68]. In this regard, the erosive Kula badland topography most likely responds to fault development evolved by both gravitational potential energy difference and tectonic boundary conditions in the Kula Basin.

5.3. Potential Triggers and Controlling Factors

Based on the field evidence presented in this work, it is likely that;

- Lithological variety, particularly the presence of visibly erodible clay-sized sediments of the Ahmetler Formation contributing to rock-mass weakening, is regarded as a conditioning factor,
- The existing fold structure (i.e., the orientation of bedding, folds) serves as the conditioning factor as it prepares the basin for preferential water flow in the palaeo- and present-day topography,
- Faulting and its geometry work as a controlling factor as different orientated faults generate (i) combined erosion/sedimentation surfaces and (ii) morphological patterns for water flow in the form of deepened gullies.

A few pottery pieces, of possibly Ancient Greek to Byzantine origin, observed in the fluvial units close to heights to the current incision levels, suggest several cyclic transport-sedimentation periods, at least during the past few thousands of years in sub-catchments. As mentioned in the introduction, it is suggested that there were several wet periods during the reign of the Byzantine Empire in West and Central Anatolia that influenced their agricultural practices [82]. Although it is not the main objective of this study, it is likely that such wet periods, which influenced the erosion-sedimentation dynamics and gully growth [37], possibly act as a climate change-related conditioning factor for the badland development.

6. Conclusions

This work demonstrates the impact of structural control in Quaternary surface dynamics of an extensively erosive badland landscape between the Kula and Selendi Towns, western Turkey. We tested the hypothesis that fault activity and rock structure have significant influence on syn-kinematic erosion/sedimentation dynamics and morphological evolution of the extensional tectonic regime of the Kula Basin. The data we collected has demonstrated a link between NW-SE- and NE-SW-orientated faulting in an asymmetric extensional tectonic basin and Quaternary erosion and sediment preservation with field evidence. The methodology is primarily based on field survey with geological and structural mapping in the entire study area, combined with morphometric analysis of the landscape using a DEM.

The lithological units, consisting of relatively erodible clay-sized material, make this area susceptible to extensive erosion, leading to the development of the badlands in between plateaux. Extension-related faulting and footwall exhumation significantly contribute to erosion-deposition at fault-determined locations with gradual faulting. The normal faulting provides accommodation space in the hanging wall in response to the eroded sediments in the footwall of normal faults. We also acknowledge the influence of the faulting geometry and gentle folding in palaeo, and current water flow direction and gully deepening in the basin.

The fieldwork-based multidisciplinary methodology of this study shows the importance of fundamental geological field mapping combined with morphometric analysis, to understand the interaction between structural control and surface dynamics in an erosive landscape.
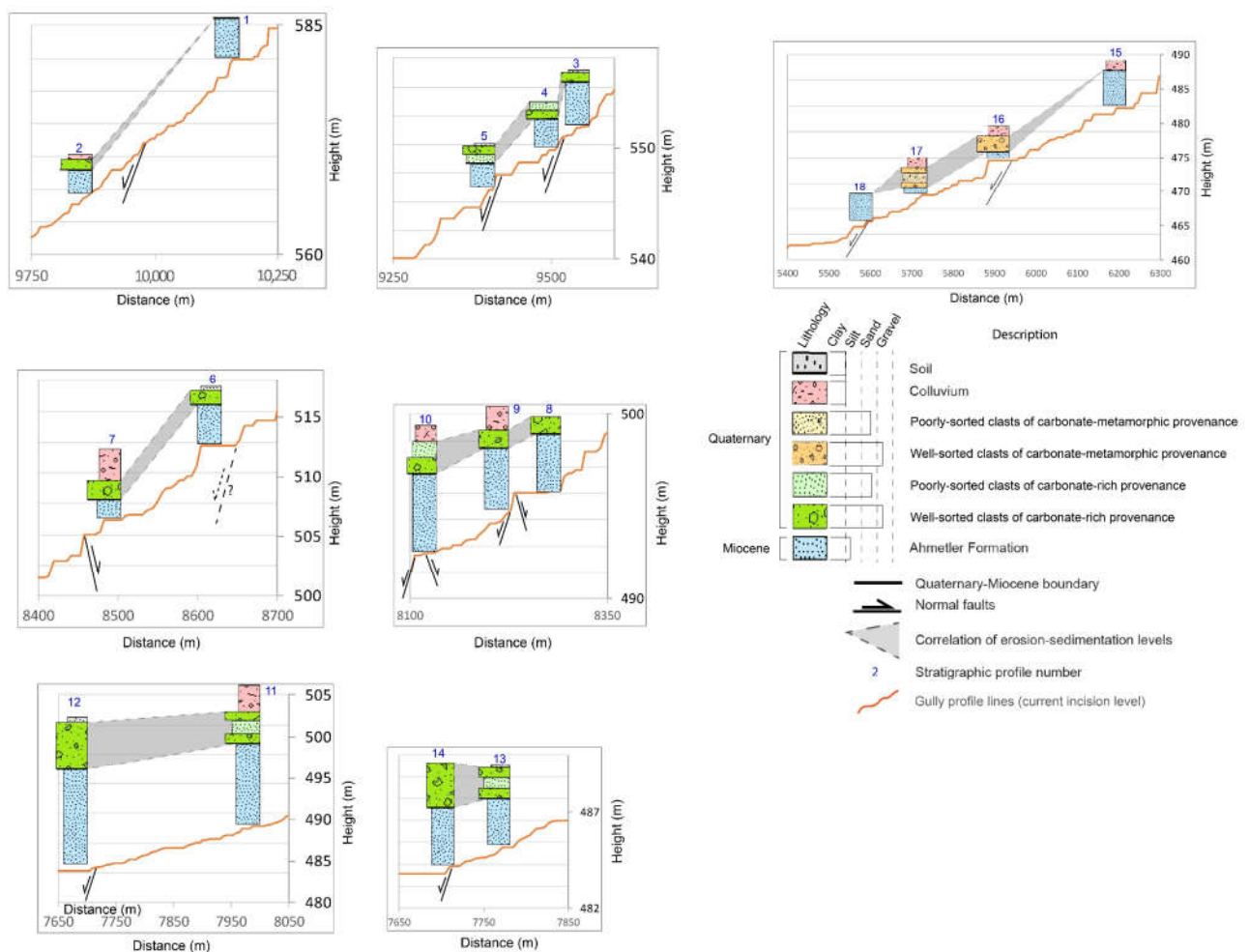
Appendix A

Figure A1. Correlated Quaternary sedimentary units are shown with stratigraphic logs with their position in the gully, current incision levels, faults and their textural differences. Stratigraphic columns 1–14 are from gully Z1, and columns 15–18 are from gully X in Figure 5. Stratigraphic columns (from 1 to 18) are explained in Table 1.

References

1. Bryan, R.; Yair, A. *Badland: Geomorphology and Piping*; Geo Books: Norwich, UK, 1982.
2. Kašanin-Grubin, M.; Vergari, F.; Troiani, F.; Della Seta, M. The Role of Lithology. In *Badlands Dynamics in a Context of Global Change*; Elsevier: Amsterdam, The Netherlands, 2018; pp. 61–109. ISBN 9780128130544.
3. Joshi, V.U.; Nagare, V.B. Badland formation along the Pravara River, Western Deccan, India. Can neotectonics be the cause? *Z. Geomorphol.* **2013**, *57*, 349–370. [CrossRef]
4. Van Gorp, W.; Veldkamp, A.; Temme, A.J.A.M.; Maddy, D.; Demir, T.; van der Schriek, T.; Reimann, T.; Wallinga, J.; Wijbrans, J.; Schoorl, J.M. Fluvial response to Holocene volcanic damming and breaching in the Gediz and Geren rivers, western Turkey. *Geomorphology* **2013**, *201*, 430–448. [CrossRef]
5. Ranga, V.; Mohapatra, S.N.; Pani, P. Geomorphological evolution of badlands based on the dynamics of palaeo-channels and their implications. *J. Earth Syst. Sci.* **2015**, *124*, 909–920. [CrossRef]
6. Martínez-Murillo, J.F.; Nadal-Romero, E. Perspectives on Badland Studies in the Context of Global Change. In *Badlands Dynamics in a Context of Global Change*; Elsevier: Amsterdam, The Netherlands, 2018; pp. 1–25. ISBN 9780128130544.
7. Torri, D.; Rossi, M.; Brogi, F.; Marignani, M.; Bacaro, G.; Santi, E.; Tordoni, E.; Amici, V.; Maccherini, S. Badlands and the dynamics of human history, land use, and vegetation through centuries. In *Badlands Dynamics in a Context of Global Change*; Elsevier: Amsterdam, The Netherlands, 2018; pp. 111–153. ISBN 9780128130544.
8. Boardman, J.; Parsons, A.J.; Holland, R.; Holmes, P.J.; Washington, R. Development of badlands and gullies in the Sneeuberg, Great Karoo, South Africa. *CATENA* **2003**, *50*, 165–184. [CrossRef]

9. Nadal-Romero, E.; Latron, J.; Martí-Bono, C.; Regüés, D. Temporal distribution of suspended sediment transport in a humid Mediterranean badland area: The Araguás catchment, Central Pyrenees. *Geomorphology* **2008**, *97*, 601–616. [CrossRef]
10. Moreno-de Las Heras, M.; Gallart, F. The origin of badlands. In *Badlands Dynamics in a Context of Global Change*; Elsevier: Amsterdam, The Netherlands, 2018; pp. 27–59. ISBN 9780128130544.
11. Moretti, S.; Rodolfi, G. A typical "calanchi" landscape on the Eastern Apennine margin (Atri, Central Italy): Geomorphological features and evolution. *CATENA* **2000**, *40*, 217–228. [CrossRef]
12. Nadal-Romero, E.; Vicente-Serrano, S.M.; Jiménez, I. Assessment of badland dynamics using multi-temporal Landsat imagery: An example from the Spanish Pre-Pyrenees. *CATENA* **2012**, *96*, 1–11. [CrossRef]
13. Hevia, J.N.; de Araújo, J.C.; Manso, J.M. Assessment of 80 years of ancient-badlands restoration in saldaña, Spain. *Earth Surf. Process. Landf.* **2014**, *39*, 1563–1575. [CrossRef]
14. Vericat, D.; Smith, M.W.; Brasington, J. Patterns of topographic change in sub-humid badlands determined by high resolution multi-temporal topographic surveys. *CATENA* **2014**, *120*, 164–176. [CrossRef]
15. Bentivenga, M.; Agosta, F.; Palladino, G.; Piccarreta, M.; Prosser, G. Structural control on badland slope evolution: A case study from the southern Apennines (Italy). *Geomorphology* **2021**, *374*, 107518. [CrossRef]
16. Bentivenga, M.; Capolongo, D.; Palladino, G.; Piccarreta, M. Geomorphological map of the area between Craco and Pisticci (Basilicata, Italy). *J. Maps* **2015**, *11*, 267–277. [CrossRef]
17. Agarwal, K.; Singh, I.; Sharma, M.; Sharma, S.; Rajagopalan, G. Extensional tectonic activity in the cratonward parts (peripheral bulge) of the Ganga Plain foreland basin, India. *Int. J. Earth Sci.* **2002**, *91*, 897–905. [CrossRef]
18. Densmore, A.L. Footwall topographic development during continental extension. *J. Geophys. Res.* **2004**, *109*, F03001. [CrossRef]
19. Cowie, P.A.; Attal, M.; Tucker, G.E.; Whittaker, A.C.; Naylor, M.; Ganas, A.; Roberts, G.P. Investigating the surface process response to fault interaction and linkage using a numerical modelling approach. *Basin Res.* **2006**, *18*, 231–266. [CrossRef]
20. Whittaker, A.C.; Attal, M.; Allen, P.A. Characterising the origin, nature and fate of sediment exported from catchments perturbed by active tectonics. *Basin Res.* **2010**, *22*, 809–828. [CrossRef]
21. Vanmaercke, M.; Kettner, A.J.; van Den Eeckhaut, M.; Poesen, J.; Mamaliga, A.; Verstraeten, G.; Rãdoane, M.; Obreja, F.; Upton, P.; Syvitski, J.P.M.; et al. Moderate seismic activity affects contemporary sediment yields. *Prog. Phys. Geogr.* **2014**, *38*, 145–172. [CrossRef]
22. Graveleau, F.; Strak, V.; Dominguez, S.; Malavieille, J.; Chatton, M.; Manighetti, I.; Petit, C. Experimental modelling of tectonics-erosion-sedimentation interactions in compressional, extensional, and strike-slip settings. *Geomorphology* **2015**, *244*, 146–168. [CrossRef]
23. Veldkamp, A.; Van den Berg, M.W.; Van Dijke, J.J.; Van den Berg van Saparoea, R.M. Reconstructing Late Quaternary fluvial process controls in the upper Aller Valley (North Germany) by means of numerical modeling. *Neth. J. Geosci.* **2002**, *81*, 375–388. [CrossRef]
24. Schoorl, J.M.; Temme, A.J.A.M.; Veldkamp, T. Modelling centennial sediment waves in an eroding landscape—Catchment complexity. *Earth Surf. Process. Landf.* **2014**, *39*, 1526–1537. [CrossRef]
25. Lima, C.C.U.; Bezerra, F.H.R.; Nogueira, F.C.C.; Maia, R.P.; Sousa, M.O.L. Quaternary fault control on the coastal sedimentation and morphology of the São Francisco coastal plain, Brazil. *Tectonophysics* **2014**, *633*, 98–114. [CrossRef]
26. Hack, J.T. Stream-profile analysis and stream-gradient index. *J. Res. US Geol. Surv.* **1973**, *1*, 421–429.
27. Seeber, L.; Gornitz, V. River profiles along the Himalayan arc as indicators of active tectonics. *Tectonophysics* **1983**, *92*, 335–367. [CrossRef]
28. Crosby, B.T.; Whipple, K.X. Knickpoint initiation and distribution within fluvial networks: 236 waterfalls in the Waipaoa River, North Island, New Zealand. *Geomorphology* **2006**, *82*, 16–38. [CrossRef]
29. Kirby, E.; Whipple, K.X. Expression of active tectonics in erosional landscapes. *J. Struct. Geol.* **2012**, *44*, 54–75. [CrossRef]
30. Demoulin, A.; Mather, A.; Whittaker, A. Fluvial archives, a valuable record of vertical crustal deformation. *Quat. Sci. Rev.* **2017**, *166*, 10–37. [CrossRef]
31. Babaei, S.; Dehbozorgi, M.; Hosseiniasl, A.; Hakimi Asiabar, S. New insights into the effect of the quaternary fault activity on river knickpoints in the Central Alborz (Iran). *Quat. Int.* **2020**, *562*, 104–120. [CrossRef]
32. Viveen, W.; Baby, P.; Hurtado-Enríquez, C. Assessing the accuracy of combined DEM-based lineament mapping and the normalised SL-index as a tool for active fault mapping. *Tectonophysics* **2021**, *813*, 228942. [CrossRef]
33. UNESCO. Global Geoparks. Available online: http://www.unesco.org/new/en/natural-sciences/environment/earth-sciences/unesco-global-geoparks/list-of-unesco-global-geoparks/turkey/kula-volcanic/ (accessed on 15 August 2020).
34. Erinç, S. The young volcanic topography of the Kula-Adala area. *Istanb. Univ. Cografya Enst. Dergisi* **1970**, *17*, 7–22.
35. Maddy, D.; Demir, T.; Bridgland, D.R.; Veldkamp, A.; Stemerdink, C.; van der Schriek, T.; Schreve, D. The Pliocene initiation and Early Pleistocene volcanic disruption of the palaeo-Gediz fluvial system, Western Turkey. *Quat. Sci. Rev.* **2007**, *26*, 2864–2882. [CrossRef]
36. Veldkamp, A.; Baartman, J.E.M.; Coulthard, T.J.; Maddy, D.; Schoorl, J.M.; Storms, J.E.A.; Temme, A.J.A.M.; van Balen, R.; van De Wiel, M.J.; van Gorp, W.; et al. Two decades of numerical modelling to understand long term fluvial archives: Advances and future perspectives. *Quat. Sci. Rev.* **2017**, *166*, 177–187. [CrossRef]
37. Van Gorp, W.; Temme, A.J.A.M.; Veldkamp, A.; Schoorl, J.M. Modelling long-term (300 ka) upland catchment response to multiple lava damming events. *Earth Surf. Process. Landf.* **2015**, *40*, 888–900. [CrossRef]

38. Bunbury, J.M.; Hall, L.; Anderson, G.J.; Stannard, A. The determination of fault movement history from the interaction of local drainage with volcanic episodes. *Geol. Mag.* **2001**, *138*, 185–192. [CrossRef]

39. Ercan, T.; Türkecan, A.; Mengü, A.; Günay, E. Kula-Selendi (Manisa) Dolaylarının Jeolojisi. *Jeol. Muhendis.* **1983**, *17*, 3–28.

40. Westaway, R.; Guillou, H.; Yurtmen, S.; Beck, A.; Bridgland, D.; Demir, T.; Scaillet, S.; Rowbotham, G. Late Cenozoic uplift of western Turkey: Improved dating of the Kula Quaternary volcanic field and numerical modelling of the Gediz River terrace staircase. *Glob. Planet. Change* **2006**, *51*, 131–171. [CrossRef]

41. Heineke, C.; Niedermann, S.; Hetzel, R.; Akal, C. Surface exposure dating of Holocene basalt flows and cinder cones in the Kula volcanic field (Western Turkey) using cosmogenic 3He and 10Be. *Quat. Geochronol.* **2016**, *34*, 81–91. [CrossRef]

42. Yilmaz, Y.; Genç, Ş.C.; Gürer, F.; Bozcu, M.; Yilmaz, K.; Karacik, Z.; Altunkaynak, Ş.; Elmas, A. When did the western Anatolian grabens begin to develop? *Geol. Soc. Spec. Publ.* **2000**, *173*, 353. [CrossRef]

43. Westaway, R.; Pringle, M.; Yurtmen, S.; Demir, T.; Bridgland, D.; Rowbotham, G.; Maddy, D. Pliocene and Quaternary Regional Uplift in Western Turkey: The Gediz River Terrace Staircase and the Volcanism at Kula. *Tectonophysics* **2004**, *391*, 121–169. [CrossRef]

44. Maddy, D.; Veldkamp, A.; Jongmans, A.G.; Candy, I.; Demir, T.; Schoorl, J.M.; van der Schriek, T.; Stemerdink, C.; Scaife, R.G.; van Gorp, W. Volcanic disruption and drainage diversion of the palaeo-Hudut River, a tributary of the Early Pleistocene Gediz River, Western Turkey. *Geomorphology* **2012**, *165*, 62–77. [CrossRef]

45. Maddy, D.; Demir, T.; Bridgland, D.R.; Veldkamp, A.; Stemerdink, C.; van der Schriek, T.; Westaway, R. An obliquity-controlled Early Pleistocene river terrace record from Western Turkey? *Quat. Res.* **2005**, *63*, 339–346. [CrossRef]

46. Maddy, D.; Veldkamp, A.; Demir, T.; Aytaç, A.S.; Schoorl, J.M.; Scaife, R.; Boomer, I.; Stemerdink, C.; van der Schriek, T.; Aksay, S.; et al. Early Pleistocene River Terraces of the Gediz River, Turkey: The role of faulting, fracturing, volcanism and travertines in their genesis. *Geomorphology* **2020**, *358*, 107102. [CrossRef]

47. Van Gorp, W.; Temme, A.J.A.M.; Baartman, J.E.M.; Schoorl, J.M. Landscape evolution modelling of naturally dammed rivers. *Earth Surf. Process. Landf.* **2014**, *39*, 1587–1600. [CrossRef]

48. Maddy, D.; Veldkamp, A.; Demir, T.; van Gorp, W.; Wijbrans, J.R.; van Hinsbergen, D.J.J.; Dekkers, M.J.; Schreve, D.; Schoorl, J.M.; Scaife, R.; et al. The Gediz River fluvial archive: A benchmark for Quaternary research in Western Anatolia. *Quat. Sci. Rev.* **2017**, *166*, 289–306. [CrossRef]

49. Ercan, T. Interpretation of Geochemical, Radiometric and Isotopic Data on Kula Volcanics (Manisa—W. Anatolia). *Türk. Jeol. Bül.* **1993**, *36*, 113–129.

50. Taymaz, T.; Tan, O.; Yolsal, S. Active Tectonics of Turkey and Surroundings and Seismic Risk in the Marmara Sea Region. In Proceedings of the IWAM04, Mizunami, Japan, 31 March 2004.

51. Şengör, A.M.C.; Tüysüz, O.; İmren, C.; Sakınç, M.; Eyidoğan, H.; Görür, N.; Le Pichon, X.; Rangin, C. The North Anatolian Fault: A new look. *Annu. Rev. Earth Planet. Sci.* **2005**, *33*, 37–112. [CrossRef]

52. Le Pichon, X.; Imren, C.; Rangin, C.; Şengör, A.M.C.; Siyako, M. The South Marmara Fault. *Int. J. Earth Sci.* **2014**, *103*, 219–231. [CrossRef]

53. Özbakir, A.D.; Govers, R.; Wortel, R. Active faults in the Anatolian-Aegean plate boundary region with Nubia. *Turk. J. Earth Sci.* **2017**, *26*, 30–56. [CrossRef]

54. European Environment Agency European Environment Agency (EEA). Available online: https://land.copernicus.eu/imagery-in-situ/eu-dem/eu-dem-v1.1/view (accessed on 3 March 2020).

55. USGS Earthquake Catalog. Available online: https://earthquake.usgs.gov/earthquakes/search/ (accessed on 28 July 2020).

56. Avcıoğlu, A.; Görüm, T.; Akbaş, A.; Moreno-de las Heras, M.; Yıldırım, C.; Yetemen, Ö. Regional distribution and characteristics of major badland landscapes in Turkey. *CATENA* **2022**, *218*, 106562. [CrossRef]

57. Fick, S.E.; Hijmans, R.J. WorldClim 2: New 1-km spatial resolution climate surfaces for global land areas. *Int. J. Climatol.* **2017**, *37*, 4302–4315. [CrossRef]

58. USGS ComCat Earthquake Hazards Program. The ANSS Comprehensive Earthquake Catalog (ComCat). Available online: http://earthquake.usgs.gov/earthquakes/search/ (accessed on 20 May 2021).

59. Bozkurt, E. Origin of NE-trending basins in western Turkey. *Geodin. Acta* **2003**, *16*, 61–81. [CrossRef]

60. Purvis, M.; Robertson, A. A pulsed extension model for the Neogene-Recent E-W-trending Alaşehir Graben and the NE-SW-trending Selendi and Gördes Basins, Western Turkey. *Tectonophysics* **2004**, *391*, 171–201. [CrossRef]

61. Ersoy, Y.E.; Helvaci, C.; Sözbilir, H. Tectono-stratigraphic evolution of the NE-SW-trending superimposed Selendi basin: Implications for late Cenozoic crustal extension in Western Anatolia, Turkey. *Tectonophysics* **2010**, *488*, 210–232. [CrossRef]

62. Çiftçi, N.B.; Bozkurt, E. Structural evolution of the Gediz Graben, SW Turkey: Temporal and spatial variation of the graben basin. *Basin Res.* **2010**, *22*, 846–873. [CrossRef]

63. McKenzie, D. Active Tectonics of the Mediterranean Region. *Geophys. J. R. Astron. Soc.* **1972**, *30*, 109–185. [CrossRef]

64. McClusky, S.; Balassanian, S.; Barka, A.; Demir, C.; Ergintav, S.; Georgiev, I.; Gurkan, O.; Hamburger, M.; Hurst, K.; Kahle, H.; et al. Global Positioning System constraints on plate kinematics and dynamics in the eastern Mediterranean and Caucasus. *J. Geophys. Res. Solid Earth* **2000**, *105*, 5695–5719. [CrossRef]

65. McKenzie, D. The East Anatolian Fault: A major structure in Eastern Turkey. *Earth Planet. Sci. Lett.* **1976**, *29*, 189–193. [CrossRef]

66. Taymaz, T.; Jackson, J.; Westaway, R. Earthquake mechanisms in the Hellenic Trench near Crete. *Geophys. J. Int.* **1990**, *102*, 695–731. [CrossRef]

67. Ketin, I. Über die tektonisch-mechanischen Folgerungen aus den großen anatolischen Erdbeben des letzten Dezenniums. *Geol. Rundsch.* **1948**, *36*, 77–83. [CrossRef]

68. Özeren, M.S.; Holt, W.E. The dynamics of the eastern Mediterranean and eastern Turkey. *Geophys. J. Int.* **2010**, *183*, 1165–1184. [CrossRef]

69. Dewey, J.F.; Şengör, A.M.C. Aegean and surrounding regions: Complex multiplate and continuum tectonics in a convergent zone. *Bull. Geol. Soc. Am.* **1979**, *90*, 84–92. [CrossRef]

70. Le Pichon, X. Land-locked oceanic basins and continental collision: The Eastern Mediterranean as a case example. *Mt. Build. Process.* **1982**, 201–211. [CrossRef]

71. Seyitoğlu, G. Late Cenozoic tectono-sedimentary development of the Selendi and Uşak-Güre basins: A contribution to the discussion on the development of east–west and north trending basins in western Turkey. *Geol. Mag.* **1997**, *134*, 163–175. [CrossRef]

72. Bozkurt, E. Neotectonics of Turkey—A synthesis. *Geodin. Acta* **2001**, *14*, 3–30. [CrossRef]

73. Bozkurt, E.; Sözbilir, H. Tectonic evolution of the Gediz Graben: Field evidence for an episodic, two-stage extension in western Turkey. *Geol. Mag.* **2004**, *141*, 63–79. [CrossRef]

74. Purvis, M.; Robertson, A. Miocene sedimentary evolution of the NE-SW-trending Selendi and Gördes Basins, W Turkey: Implications for extensional processes. *Sediment. Geol.* **2005**, *174*, 31–62. [CrossRef]

75. Koçyiğit, A.; Yusufoğlu, H.; Bozkurt, E. Evidence from the Gediz graben for episodic two-stage extension in western Turkey. *J. Geol. Soc.* **1999**, *156*, 605. [CrossRef]

76. Seyitoglu, G.; Cemen, I.; Tekeli, O. Extensional folding in the Alasehir (Gediz) graben, western Turkey. *J. Geol. Soc.* **2000**, *157*, 1097. [CrossRef]

77. Çiftçi, N.B.; Bozkurt, E. Folding of the Gediz Graben fill, SW Turkey: Extensional and/or contractional origin? *Geodin. Acta* **2008**, *21*, 145–167. [CrossRef]

78. Şengör, A.M.C.; Bozkurt, E. Layer-parallel shortening and related structures in zones undergoing active regional horizontal extension. *Int. J. Earth Sci.* **2013**, *102*, 101–119. [CrossRef]

79. Maddy, D.; Demir, T.; Veldkamp, A.; Bridgland, D.R.; Stemerdink, C.; Van Der Schriek, T.; Schreve, D. The obliquity-controlled early Pleistocene terrace sequence of the Gediz River, western Turkey: A revised correlation and chronology. *J. Geol. Soc.* **2012**, *169*, 67–82. [CrossRef]

80. Veldkamp, A.; Candy, I.; Jongmans, A.G.; Maddy, D.; Demir, T.; Schoorl, J.M.; Schreve, D.; Stemerdink, C.; van der Schriek, T. Reconstructing Early Pleistocene (1.3 Ma) terrestrial environmental change in western Anatolia: Did it drive fluvial terrace formation? *Palaeogeogr. Palaeoclimatol. Palaeoecol.* **2015**, *417*, 91–104. [CrossRef]

81. Ozaner, F.S. Detecting the polycyclic drainage evolution in Kula region (western Turkey) using aerial photographs. *ITC J.* **1992**, *3*, 249–253.

82. Haldon, J.; Roberts, N.; Izdebski, A.; Fleitmann, D.; McCormick, M.; Cassis, M.; Doonan, O.; Eastwood, W.; Elton, H.; Ladstätter, S.; et al. The climate and environment of Byzantine Anatolia: Integrating science, history, and archaeology. *J. Interdiscipl. Hist.* **2014**, *45*, 113–161. [CrossRef]

83. Şen, E.; Aydar, E.; Bayhan, H.; Gourgaud, A. Alkali bazalt ve piroklastik çökellerin volkanolojik özellikleri, kula volkanları, batı anadolu. *Yerbilim. Earth Sci.* **2014**, *35*, 219–252. [CrossRef]

84. Lazzari, M. High-Resolution LiDAR-Derived DEMs in Hydrografic Network Extraction and Short-Time Landscape Changes. *Lect. Notes Comput. Sci.* **2020**, *12250*, 723–737. [CrossRef]

85. Allmendinger, R.W.; Cardozo, N.; Fisher, D.M. *Structural Geology Algorithms: Vectors and Tensors*; Cambridge University Press: Cambridge, UK, 2011; ISBN 9780511920202.

86. Cardozo, N.; Allmendinger, R.W. Spherical projections with OSXStereonet. *Comput. Geosci.* **2013**, *51*, 193–205. [CrossRef]

87. Pérez-Peña, J.V.; Azañón, J.M.; Azor, A.; Delgado, J.; González-Lodeiro, F. Spatial analysis of stream power using GIS: SLk anomaly maps. *Earth Surf. Process. Landf.* **2009**, *34*, 16–25. [CrossRef]

88. El Hamdouni, R.; Irigaray, C.; Fernández, T.; Chacón, J.; Keller, E.A. Assessment of relative active tectonics, southwest border of the Sierra Nevada (southern Spain). *Geomorphology* **2008**, *96*, 150–173. [CrossRef]

89. Bull, W.B. *Tectonic Geomorphology of Mountains: A New Approach to Paleoseismology*; Blackwell: Oxford, UK, 2007; p. 316.

90. Ghosh, S.; Sivakumar, R. Assessment of morphometric parameters for the development of Relative Active Tectonic Index and its significant for seismic hazard study: An integrated geoinformatic approach. *Environ. Earth Sci.* **2018**, *77*, 600. [CrossRef]

91. Aksay, S.; Schoorl, J.; Veldkamp, A.; Demir, T.; Aytaç, S.; Maddy, D. The influence of structural control in erosion-sedimentation dynamics and morphology of a badland topography. EGU22-11870. In Proceedings of the EGU General Assembly 2022, Vienna, Austria, 23–27 May 2022.

92. Sözbilir, H. Extensional Tectonics and the Geometry of Related Macroscopic Structures: Field Evidence from the Gediz Detachment, Western Turkey. *Turk. J. Earth Sci.* **2001**, *10*, 51–67.

93. Andrić, N.; Sant, K.; Matenco, L.; Mandic, O.; Tomljenović, B.; Pavelić, D.; Hrvatović, H.; Demir, V.; Ooms, J. The link between tectonics and sedimentation in asymmetric extensional basins: Inferences from the study of the Sarajevo-Zenica Basin. *Mar. Pet. Geol.* **2017**, *83*, 305–332. [CrossRef]

94. García-García, F.; Fernández, J.; Viseras, C.; Soria, J.M. Architecture and sedimentary facies evolution in a delta stack controlled by fault growth (Betic Cordillera, southern Spain, late Tortonian). *Sediment. Geol.* **2006**, *185*, 79–92. [CrossRef]

95. Hovius, N.; Meunier, P.; Lin, C.W.; Chen, H.; Chen, Y.G.; Dadson, S.; Horng, M.J.; Lines, M. Prolonged seismically induced erosion and the mass balance of a large earthquake. *Earth Planet. Sci. Lett.* **2011**, *304*, 347–355. [CrossRef]